Journal of Geomorphology
Stuttgart, July 2023

Suitability of terrestrial archival imagery for SfM-MVS based surface reconstruction of steep rock walls for the detection of rockfalls

Kerstin Wegner[1,*], Manuel Stark[1], Florian Haas[1], Michael Becht[1]

[1] Chair of Physical Geography, Catholic University of Eichstätt-Ingolstadt, Eichstätt, 85072, Germany
* Corresponding author: kwegner@ku.de

With 12 figures and 7 tables

Abstract: Rockfalls are a common geomorphological process on steep rock slopes and therefore play an important role in the geomorphological dynamics of high mountain regions. Using multi-temporal high-resolution terrain models (DTMs) generated from remote sensing data from Light Detection and Ranging (LiDAR) and Structure-from-Motion (SfM) photogrammetry, surface changes can be calculated using a DTM of Difference (DoD). Whereas surface changes can usually only be covered over short investigation periods with terrestrial laser scanning (TLS) and digital photogrammetry, historical data sets enable surface reconstruction far back into the past. Therefore, our work focuses on the combined use of TLS data, terrestrial digital and terrestrial historical images to quantify rockfalls on the steep rock faces of the *Tre Cime di Lavaredo* in the Dolomites, Italy. The reconstruction of the topography of the rock faces from past times was preceded by an intense and time-consuming search for historical terrestrial photographs. After a complex data preparation and the development of a processing workflow adapted to the data, we were able to quantify the surface changes caused by rockfalls for the observation period 1970–2018. For two areas, we calculated surface changes of -101.28 m³ and -1,872.87 m³. Our study demonstrates the potential and limitations of historical terrestrial images for a long-term geomorphic change detection analysis of rockfalls. This specific workflow, depending on the quality of the images, has to be adapted for each dataset while constant controls of the intermediate results are indispensable.

Keywords: historical terrestrial images; lidar; terrestrial laser scanning; structure from motion; rockfalls; long-term change detection

1 Introduction

The shaping of the landscape by geomorphological processes is particularly visible in high mountains, in which a multitude of individual processes and their interaction are involved. The magnitude and frequency of these processes are determined by relief and climate forcing. This process, driven e.g. by frost weathering, transports material from the rock faces to the associated scree slopes (e.g. Hungr & Evans 1988, Krautblatter & Dikau 2017). Due to the anthropogenic use of these landscapes, frequently occurring gravitational processes, in particular, pose a major threat to infrastructures and settlement areas (e.g. Pfeiffer & Bowen 1989, Ravanel et al. 2010, Volkwein et al. 2011, Frattini et al. 2012, Heiser et al. 2017, Vanneschi et al. 2019). This shows the high importance of evaluating the process dynamics of such events in the context of natural hazard analysis. Based on the combination of climatic forcing and process dynamics, the dynamics of geomorphic processes of high alpine geosystems are highly sensitive to climate variability (e.g. Magnin et al. 2017, Gallach et al. 2020, Legay et al. 2021). Consequently, changes in air temperature and precipitation inevitably affect geomorphodynamics and thus rockfall processes (Paranunzio et al. 2016, Gallach et al. 2020, Legay et al. 2021). In particular, thawing of permafrost leads to instability of the rock faces and mountain slopes (Ravanel & Deline 2010, Viero et al. 2013, Paranunzio et al. 2016, Gallach et al. 2020, IPCC 2021, Legay et al. 2021)

LiDAR (light detection and ranging) techniques, either airborne laser scanning (ALS) or terrestrial laser scanning (TLS), can be used to obtain precise topographic information to determine process variables and process areas (e.g. Abellán et al. 2011, Haas et al. 2012, Heckmann et al. 2012, Salvini et al. 2013, Royán et al.

DOI: 10.1127/jgeomorphology/2023/0775

Gebrüder Borntraeger Science Publishers, Stuttgart, www.borntraeger-cramer.de

2014, Strunden et al. 2015, Obanawa & Hayakawa 2018, Sala et al. 2019, Guerin et al. 2020a, b). Since data acquisition is coupled with high equipment and survey costs, high temporal resolution monitoring with e.g. TLS or robot tachymeters is normally carried out in particularly endangered settings only. Therefore, such data in high mountains are only available selectively and only with poor temporal resolution.

The use of digital photogrammetric methods has recently provided geosciences with another method for recording topography. Using Structure from Motion (SfM) (Ullman 1979), 3D terrain surfaces can be reconstructed from at least two photos consisting of different perspectives with a certain degree of image overlap (Eltner et al. 2016, Linder 2016, Aber et al. 2019). SfM can be coupled with multi-view stereo (MVS) algorithms for the densification of the SfM-based 3D point clouds to reconstruct the surface in detail (Carrivick et al. 2016). Due to the cost-effective use of the technology in contrast to e.g. LiDAR measurements, higher temporal resolution can be established, which allows capturing the geomorphological process dynamics in a high resolution. Based on these advantages, SfM-MVS is used in a wide range of geosciences research, such as for the analysis of rockfall dynamics (e.g. Salvini et al. 2013, Casagli et al. 2017, Vanneschi et al. 2019, Guerin et al. 2020a, Gallo et al. 2021), the monitoring of landslides (e.g. Stumpf et al. 2015, Eker et al. 2018) or glacial process research (e.g. Vivero & Lambiel 2019, Geissler et al. 2021) and in a multitude of other research fields (e.g. Jaud et al. 2019, Laporte-Fauret 2019, Derrien et al. 2020, Hemmelder et al. 2018).

The comparison of results from long-term and short-term studies allows classifying current process rates and dynamics in a long-term context. This allows to investige the influence of climate change on geomorphodynamics over longer periods. Here, the fusion of digitised (formerly analogue) photographs, particularly historical photographs, with SfM-MVS offers the possibility to extend the investigation periods further into the past. Numerous studies already exist that focus on long-term changes of, e.g., rock glacier dynamics (e.g. Fleischer et al. 2021), glacier dynamics or morphological sediment budgets (e.g. Betz et al. 2019, Altmann et al. 2020, Stark et al. 2022) within the past decades. The data used for these studies were primarily historical aerial photographs, which are well catalogued depending on the region and in most cases are available for scientific work. Due to high slope angles and typically extreme geometries of rock faces, the use of aerial imagery to capture historical rockfall dynamics is problematic. For example, Müller et al. (2014) reported an increase of vertical errors in airborne photogrammetric digital elevation models (DEMs) in areas in >40° slope, which poses a direct limitation to the monitoring of rock cliffs with aerial photography. Guerin et al. (2020a) used for their study aerial photography to analyse and quantify rockfall events over 41 years (Guerin et al. 2020a). Likewise, Ravanel & Deline (2010, 2008) used historical photographs, laser ranging with inclinometer and terrestrial laser scanning in their studies to quantify rockfalls both before and after the LIA (Little Ice Age) on the Mont Blanc Massif. However, the images used do not have the requirements for digital photogrammetry.

When historical terrestrial images meet the requirements of the SfM-MVS algorithms it offers great potential for multitemporal DTM analysis and the analyses of geomorphological processes over time spans of several decades (Eltner et al. 2016, Guerin et al. 2020a, Stark et al. 2022). In the case of steep rock faces, the advantage of terrestrial photography lies primarily in the image-object geometry (angle between object plane and lens), which, compared to aerial photography, allows a better view and consequently a more accurate reconstruction of the complex surface structures (Benjamin et al. 2020, Guerin et al. 2020a). Despite intensive research, we could not find any studies dealing with the analysis and quantification of rockfalls based on historical terrestrial imagery. The present study aims to close this research gap and to show that the combination of historical terrestrial photos and recent TLS data contains crucial potential and enables the analysis and quantification of rockfalls. This would provide the possibility to investigate rockfall dynamics into the past and to improve the understanding of e.g. the influence of changes in the climate forcing.

However, existing SfM-MVS processing workflows need to be adapted for such historical datasets, taking into account the diverse qualities and resolutions of the images. In addition to the technical aspects, the collection of historical terrestrial images is a major challenge, as they are usually not stored in a structured way in archives. Therefore, we choose a quite famous study area for which we would expect many existing historical images from different perspectives. Thus, we have chosen the *Tre Cime di Lavaredo* as one of the best-known rock formations in the Alps and we assumed that some suitable images are available, not only in public or war archives, but also in private archives. The present work was carried out using several historical terrestrial datasets starting from 1914 and two self-collected data sets from 2018 (terrestrial LiDAR and digital terrestrial photography).

2 Study site

The *Tre Cime di Lavaredo* are located in the northeast of Italy in the Sesto Dolomites, which belong to the Southern

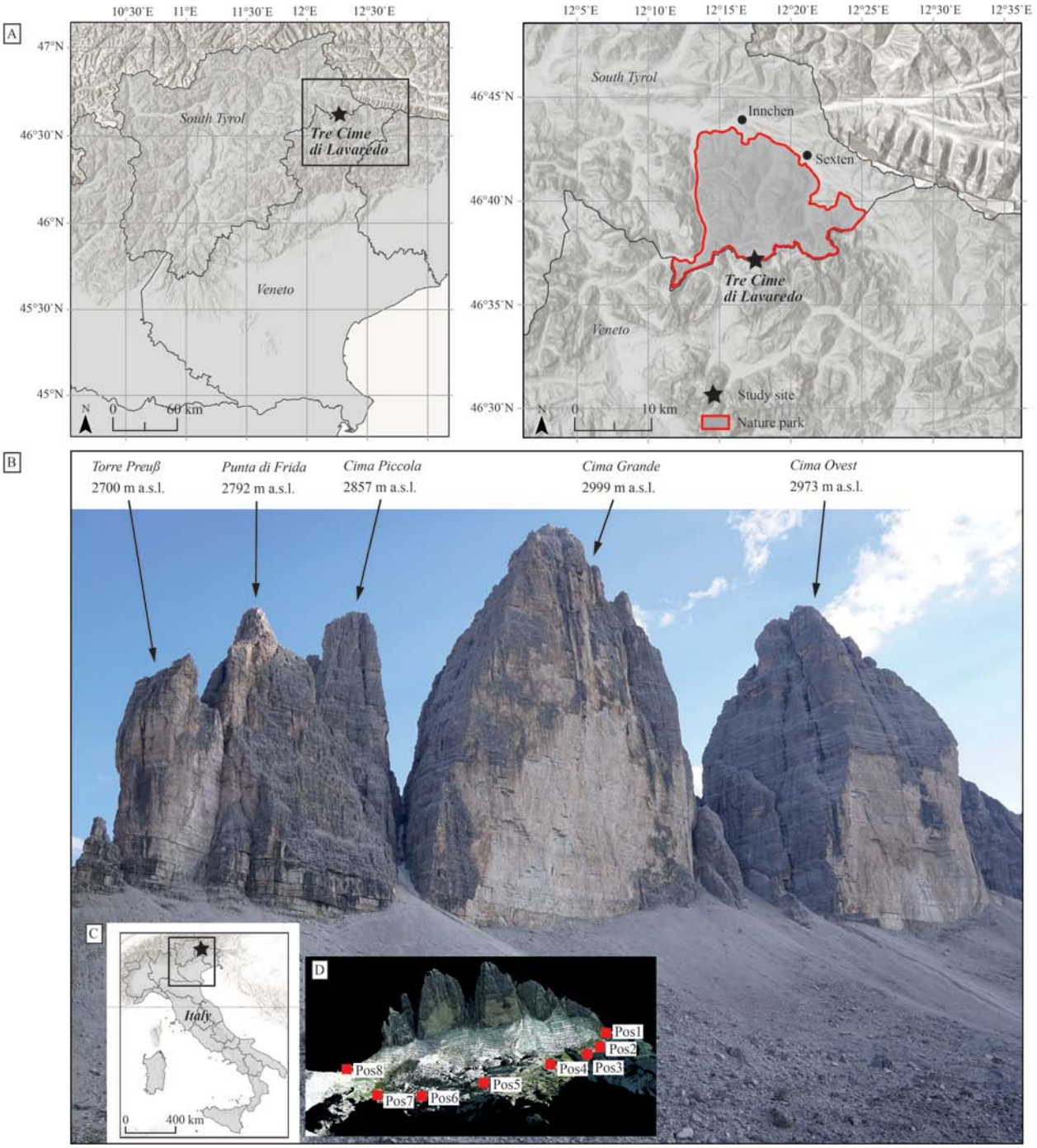

Fig. 1. Geographical location **(A, C)** of the study site (46°37′7″ N, 12°18′20″ E) and an image of the north-exposed rock faces of the *Tre Cime di Lavaredo* **(B)**. It was taken during the field campaign in July 2018 (own photo, view in south direction). **(D)** shows the eight TLS scan positions (Source of the overview base map: ESRI, HERE, Garmin, OpenStreetMap contributors and the GIS user community).

Alps and are located in the most north-eastern part of the Dolomites (Fig. 1). The massif consists of three steep vertical prominent peaks, the *Cima Grande* (2999 m a.s.l.), the *Cima Ovest* (2973 m a.s.l.) and the *Cima Piccola* (2857 m a.s.l.), which is separated into the *Punta di Frida* (2792 m a.s.l.) and the *Preußturm* (2700 m a.s.l.). Stratigraphically the Sexten Dolomites are mainly composed of dolomite ("Hauptdolomit"), which was deposited in the shallow waters of the Tethys Ocean about 200 to 220 million years ago. Their pronounced horizontal

banking gives the rock a striking horizontal structure. Vertical fissures, in combination with horizontal banking, are responsible for rock fragmentation along these faults. The edges and rock wall faces of the individual peaks also represent vertical fissure and fault surfaces. The plateau around the *Tre Cime di Lavaredo* itself is built up by the bulk Schlern dolomite. The Schlern and main dolomite are underlain by the weathering-prone and deformable Raibler layers. Their horizon, mostly composed of sandy-marly rock, shows layered or denudation terraces in the terrain and thus forms the unstable base on which the *Tre Cime di Lavaredo* stand. Consequently, retrogressive erosion of the Raibler layers also leads to destabilisation of the main dolomite rocks.

The study site is characterised by a typical alpine climate. The average annual temperature lies between 7–10°. The annual precipitation values are between 700–1000 mm (Autonome Provinz Bozen-Südtirol 2008).

The *Tre Cime di Lavaredo* are certainly one of the most important photo motifs of the Dolomites, if not of the entire European Alps. Easy access as well as the nearby refuge, allowed early touristic use. The rock faces were already a sought-after object for rock climbers at the beginning of alpinism (first ascent in 1869). Due to the multifaceted use, numerous photographs from different time periods, angles and distances exist.

3 Materials and methods

The method chapter outlines the data acquisition (TLS, terrestrial digital imagery), the archive research (historical terrestrial images) as well as a description of the processing of the different data sets with special attention to co-registration and adapted processing workflow.

3.1 Data acquisition

3.1.1 Terrestrial laser scanning

During a campaign on 27th of July 2018, we acquired TLS data with a terrestrial 3D long-range laser scanner (Riegl VZ-4000), which serves as a reference data set for the photogrammetric data and for additional analysis. The data collection took place during dry weather conditions and covered the north-facing rock walls. Due to the very complex topography of the study site, eight scan positions were acquired to minimize TLS shadowing effects (Neugirg et al. 2016) in order to capture the current topography in high resolution and with high accuracy. The data set was used as reference for the photogrammetric data and their analysis. The TLS specifications and survey parameters are given in Tables 1 and 2.

3.1.2 Terrestrial digital imagery

Simultaneously to the TLS survey, 118 terrestrial images were recorded using a Sony alpha 6000 system camera at two different height levels (chest and overhead level). The camera is equipped with a pre-calibrated sigma ILCE-6000 lens with a fixed focal length of 16 mm, yielding an absolute pixel size/pixel pitch (Eltner et al. 2016) of 4.07 µm. Aperture settings were defined automatically and were only slightly adjusted according to the light conditions. For all other survey parameters, see Table 3.

3.1.3 Archive research

An elaborate and time-consuming data research was necessary to find historical terrestrial images that meet the requirements of photogrammetric principles. Our research included official archives such as the German Alpine Association (Deutscher Alpenverein e.V., DAV) or the Office for Film and Media in Bolzano, South Tyrol, as well as online databases of Alpine and local history societies, museums and private archives. We also tried to identify the photographers of images in various books about the region (e.g. climbing books). The research yielded six data sets with an overall of 66 photographs of varying quality covering a period of more than 120 years from now. A large number of image sets did not fulfil the previously mentioned requirements of the SfM processing, such as high image overlaps (Torres-Sánchez et al. 2018), sufficient image quality (Bakker & Lane 2017) or resolution (Mosbrucker et al. 2017) and therefore, had to be excluded from the 3D object reconstruction.

Table 4 gives an overview of the historical images that were selected for further photogrammetric processing. After digitation all data were stored as digital images in uncompressed TIFF file format.

3.2 Data processing

3.2.1 Terrestrial laser scanning

Before the processing of LiDAR point clouds all artificial- and flying-points (e.g. dust, insect, birds) were manually removed. Since we were unable to install reference-points on the rock walls of the *Tre Cime di Lavaredo*, we manually co-registered the point clouds from the various scan positions (coarse registration on the base of well-distributed common points). Afterwards we used the RiSCAN PRO (Version 2.4) integrated iterative closest point (ICP) algorithm (Multi Station Adjustment tool, e.g. Zhang 1994, Micheletti et al. 2015) to finally register all scan positions to a common local reference frame (detailed description of the workflow in Haas et al. 2016) with a mean standard deviation of 0.026 m. After, the point cloud (56 million points in total; point density 20.16 points/m²) was exported in LAZ file format. To

Table 1. TLS specifications (Riegl Laser Measurement Systems GmbH, 2020). The values refer to measurements at a rate of 30 kHz (* = milliradian).

Parameter	Riegl VZ-4000
Max. measurement range	4,000 m
Min. measurement range	5 m
Field of view	60° (vertical) × 360° (horizontal)
Measurement rate	Max. 23,000 pts./s
Accuracy	15 mm
Precision	10 mm
Laser wavelength	Near-infrared
Laser beam divergence	0.15 mrad*

Table 2. TLS survey parameters.

Survey parameters	
No. of scan positions	8
Measurement frequency	30 kHz (23,000 points/s)
Humidity	30%
Temperature	24°C
Measurement distance	350–1,800 m

Table 3. Terrestrial digital imagery survey parameters.

Survey parameters	
Resolution	24.3 MP
Sensor	APS-C CMOS
Image overlap (horizontal and vertical)	>85%
Sensor-object distance	350–1,800 m

Table 4. Overview of the historical image data from archive research.

Year	Image count	Dimension [pixel]	Scan resolution [dpi]	Original format	Colour	Data source
1902–1930	6	6,520 × 4,162	1,200	Negative glass plates	greyscale	Universalarchiv der Deutschen Fotothek für Kunst- und Kulturgeschichte (Dresden, Germany)
1914	2	11,000 × 8,250	300	Negative glass plates	greyscale	Universalarchiv der Deutschen Fotothek für Kunst- und Kulturgeschichte (Dresden, Germany)
1964	7	8,315 × 8,315	1,200	Rollfilm negative	greyscale	Fotohaus Heimhuber (private archive)
1965	2	6,520 × 4,162	1,200	Rollfilm negative	greyscale	Amt für Film und Medien in Bozen, Sütirol, Italy
1970	42	8,580 × 8,800	4,000	Rollfilm negative	greyscale	Amt für Film und Medien in Bozen, Sütirol, Italy
1979	7	8,409 × 8,409	1,200	Rollfilm negative	greyscale	Fotohaus Heimhuber (private archive)

combine the LiDAR point clouds with the SfM raster datasets, we performed all further analyses in a 2.5D GIS environment. To obtain a *z*-coordinate perpendicular to the rock face, it was necessary to rotate the LiDAR point clouds (*transform pointcloud* tool in SAGA LIS, Conrad et al. 2015, Laserdata Information System, LIS: https://laserdata.at/, last access: 20.10.2022). For the georeferencing and scaling of the rock walls and the selected process areas, we extracted so-called control points (CPs) from the LiDAR point cloud. These CPs were used for all further SfM processing of historical data (see Chapter 3.2.2).

3.2.2 Image processing

Both, the historical and the high-resolution images from 2018 were processed with the same workflow (Fig. 2) with certain exceptions. Due to the significant differences between the image properties of the historical and the 2018 photo data (e.g. image quality, format, resolution, lens geometry, etc.), the settings within the SfM-MVS

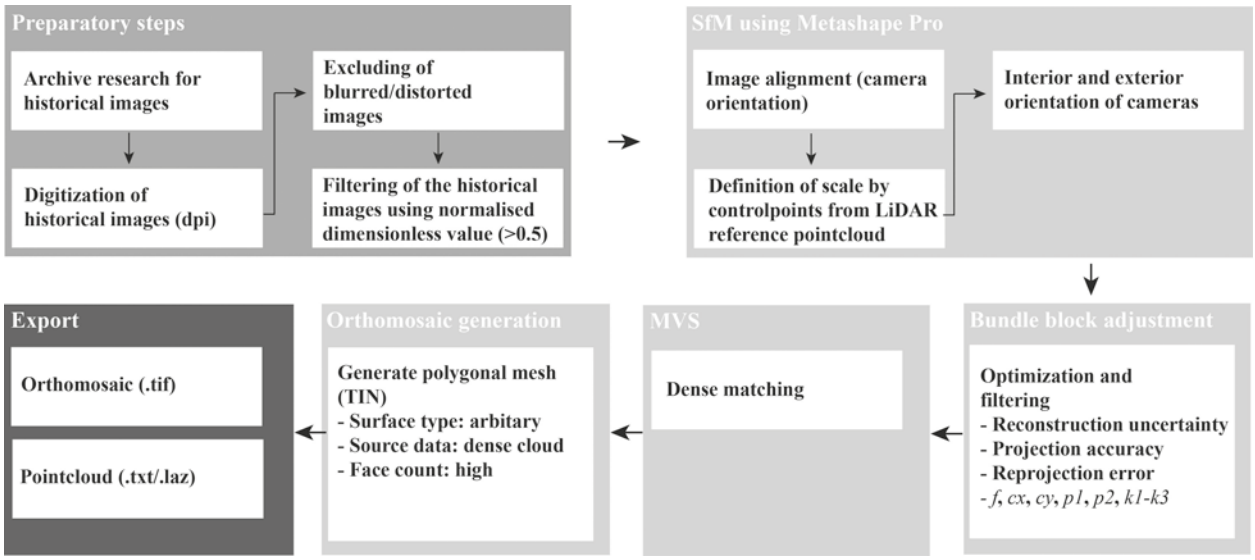

Fig. 2. Processing steps and SfM as well as MVS workflow for all images to create photomosaics and point clouds using Metashape Pro (Version 1.5.5, Agisoft LLC 2019).

processing, such as matching and densification quality, chosen camera model etc., had to be adjusted individually to the respective data set. In order to find the optimal settings, a series of test calculations were performed and the results were checked against quality and accuracy. Additionally, we filtered all images of low quality in a two-step approach. First, all blurred and fuzzy images were excluded based on visual image inspections before we applied an automatic image quality estimation (normalized dimensionless value [0;1] / 0 = low quality, 1 = high quality) within Metashape Pro (Version 1.5.5, Agisoft LLC 2019). Images with a value <0.5 were excluded from further processing. From a total of 270 photographs only six image sets (in total 66 photographs) of different dates proved to be suitable for the 3D reconstruction. All unnecessary image elements such as the sky, clouds, talus cones etc. were masked to exclude them from the image alignment.

A standard SfM-MVS workflow (Fig. 2) was performed to process all remaining images into 3D point clouds. Additionally, we calculated rectified photomosaics for all image data. The workflow contains the major steps i) camera orientation and calibration (SfM), ii) model scaling, iii) bundle block adjustments and iv) dense image matching (MVS) and is briefly described in, e.g. James et al. (2017a).

The CPs from the LiDAR data (see Chapter 3.2.1) were used to facilitate scene triangulation and reconstruction (Westoby et al. 2012) and to define and optimize exterior orientation parameters (scale, rotation and translation) of the image sets (James et al. 2017a). To improve the reconstruction quality of the photogrammetric data, different CP configurations were used and adjusted according to the respective data sets (James et al. 2017a, Tonkin & Midgley 2016, Agüera-Vega et al. 2017, Sanz-Ablanedo et al. 2018, Cabo et al. 2021). CP coordinates were extracted for structures that were readily apparent in both the LiDAR point cloud and the historical images and had not changed during the observation period. Based on careful visual observation of the respective results and the achieved RMSE of CP placement (Verma & Bourke 2019), the final parameters were chosen and the models were calculated. Due to the extreme angles between the rock faces and the camera in certain photos of the 1964/65 and 1970 data, the calculation of a model that depicts all rock faces together was abandoned and instead each rock face was calculated in a separate project of its own CP distribution (Fig. 3).

Camera parameters, such as focal length or distortion, are crucial to SfM processing. If available, these can be used to improve the results. Unfortunately, in the case of the historical terrestrial photographs no such metadata were available. Consequently, we estimated all lens parameters using the software`s internal autocalibration function. The SfM approach results in a first sparse 3D-pointcloud (tie-points) for the image data. These sparse point clouds typically contain a large number of error-prone measures which need to be filtered to improve the following bundle adjustment. Therefore, we applied certain filter operations based on the reconstruction uncertainty, projection accuracy and reprojection error for the subsequent removal of error-prone tie-points.

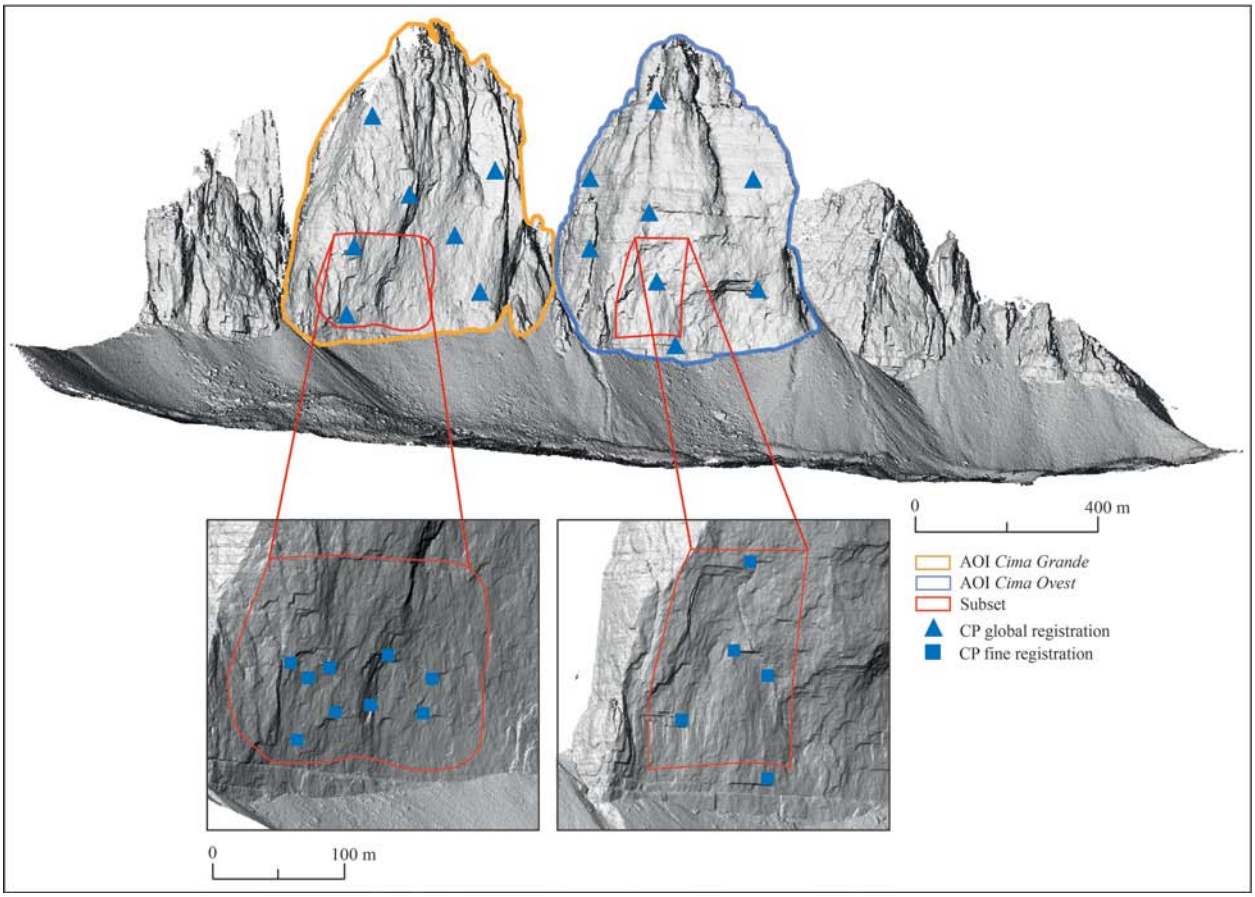

Fig. 3. Hillshade of the *Tre Cime di Lavaredo*, showing the two study areas *Cima Grande* and *Cima Ovest*. The two areas ("subset") investigated in more detail are highlighted with red polygons. Distribution of CPs on the two rock faces of *Cima Grande* and *Cima Ovest*. The triangles represent the CPs used for the first global registration step for each rock face. Using the squares, a fine registration for both rock faces was performed to increase the accuracy of the model for the corresponding area in which the rockfall occurred. View in south direction.

The projection accuracy indicates the localisation accuracy of tie-points. High reconstruction uncertainties are typical for points calculated from camera poses with a short baseline (small distance between camera positions as in the case of historical terrestrial photographs) (Agisoft LCC 2019). Together with flat angles between the projection lines of the images this can lead to high reconstruction uncertainties of the 3D coordinates. Consequently, these points can deviate considerably from the object surface, leading to noise in the photogrammetric point clouds and thus needs to be eliminated. Finally, a third filtering was used to remove points with a high reprojection error, due to poor image projections as well as by incorrect assignment of detected features. Tie-point filtering is always subject to the trade-off of removing as many poorly projected points as possible while retaining enough points with high positional accuracy to ensure seamless surface reconstruction. Although Mertes et al. (2017) and Warrick et al. (2017), among others, provide some information on the thresholds and number of tie-points used in the respective studies, they point out that no official guidelines exist in this regard and that filter settings should always depend on the given project conditions (Mayer et al. 2018). After the filtering process, the initially estimated camera parameters are optimized in the bundle adjustment. Here, the focal length (*f*), the principal point offsets in *x* and *y* coordinates (*cx, cy*) as well as radial (*k1, k2* and *k3*) and two tangential distortion coefficients (*p1, p2*) were used for the optimization before the densification of tie-points (MVS) was applied to all data. Metashape Pro provides several quality settings for the densification of tie-points. This is especially relevant to data with low resolution and poor quality as those datasets tend to produce large gaps if the quality parameters are chosen too high. The depth filter settings for detecting outliers have been set to moderate for all

Table 5. Parameter settings for SfM processing of archival image data in Metashape Pro (Version 1.5.5).

Year	Subset	Alignment quality	Marker count / RMSE [m]	Dense cloud accuracy	Depth filter
1902–1930	*Cima Grande*	Low	No alignment possible	Medium	Moderate
	Cima Ovest				
1914	*Cima Grande*	Low	7 / 1.45	Medium	Moderate
	Cima Ovest		6 / 3.14		
1964	*Cima Grande*	Medium	6 / 1.83	High	Moderate
1965	*Cima Ovest*	Medium	6 / 2.08	High	Moderate
1970	*Cima Piccola*	Medium	10 / 0.56	High	Moderate
	Cima Grande		7 / 0.32		
	Cima Ovest		8 / 0.47		
1979	*Cima Grande*	Medium	8 / 1.94	High	Moderate
	Cima Ovest		6 / 3.57		

data (Agisoft LLC 2019). To detect and calculate volumetric changes in the rock face (along the *z*-axis) in a 2.5D approach (raster DTM), all point clouds and photomosaics were rotated along the *x*-axis and the new reference plane was spanned along the *x*- and *y*-axes. All derived point clouds were exported as ASCI.txt files and the respective rectified photomosaics were stored in uncompressed TIFF files. The entire workflow of image processing is shown in Figure 2. Table 5 summarises the parameter settings for the SfM processing of the historical datasets.

3.2.3 Two-step co-referencing of SfM and LiDAR point clouds

As we expected significant differences in resolution, accuracy and coverage of the various photogrammetric point clouds due to different data quality (James et al. 2017b, James et al. 2020, Stark et al. 2022), we aimed to minimize these differences using the ICP algorithm (see chapter 3.2.1) while taking care that the co-registration was carried out on data with similar point densities. Therefore, the LiDAR point density was adjusted (point cloud thinning) according to the density of the respective SfM point clouds. The adjustment of the individual point clouds was done for each of the *Tre Cime di Lavaredo* individually. After, we derived a first DTM of Difference (DoD) in order to identify areas with clearly visible surface changes. In total, we identified four areas for further in-depth-analyses. Despite the initial co-registration, the DTMs may still contain small systematic errors. These are minimized by a second co-registration step based on the stable surfaces near the respective process area. After, all point clouds were exported as single LAZ files for further analyses.

3.2.4 Co-referencing of photomosaics

To identify the changes on the rock faces over the epochs and match them with the results of the DoD analysis, all photomosaics were co-registered using the georeferencing function (splines) in ArcGIS Pro (version 2.7.0, Esri Inc.). This referencing was done for the areas, where clearly visible changes occurred over the observation period. Between 50–150 CPs were set per registration step to achieve a final registration accuracy of less than 0.5 m (RMSE). The photomosaic of 2018 served as reference for the co-registration. Figure 4 shows the overall workflow of the present study.

3.3 Data analysis

3.3.1 DoD analysis and LoD calculation

After the co-registration all pointclouds were imported into SAGA LIS for further processing and analysis. The point clouds were aggregated with a bilinear resampling scheme (Conrad et al. 2015) to a common DTM resolution of 0.75 m. The chosen resolution is a trade-off between the best realizable resolution and the minimum number of "no-data" cells. In the case of multiple points corresponding to one grid cell the mean *z*-value of the respective points was used for the aggregation. Additionally, hill shades were calculated for better visualisation of rock wall structures. The DTMs are then used to create DoD for the respective periods. Since all point clouds are subject to uncertainty due to data acquisition and co-registration, which is reflected in the DTMs generated from them (Haas et al. 2016), a level/ limit of detection (LoD) (e.g. Brasington et al. 2003, Lane et al. 2003, Bennett et al. 2012, Fey & Wichmann 2017) was used to separate measurement errors from actual topographic changes.

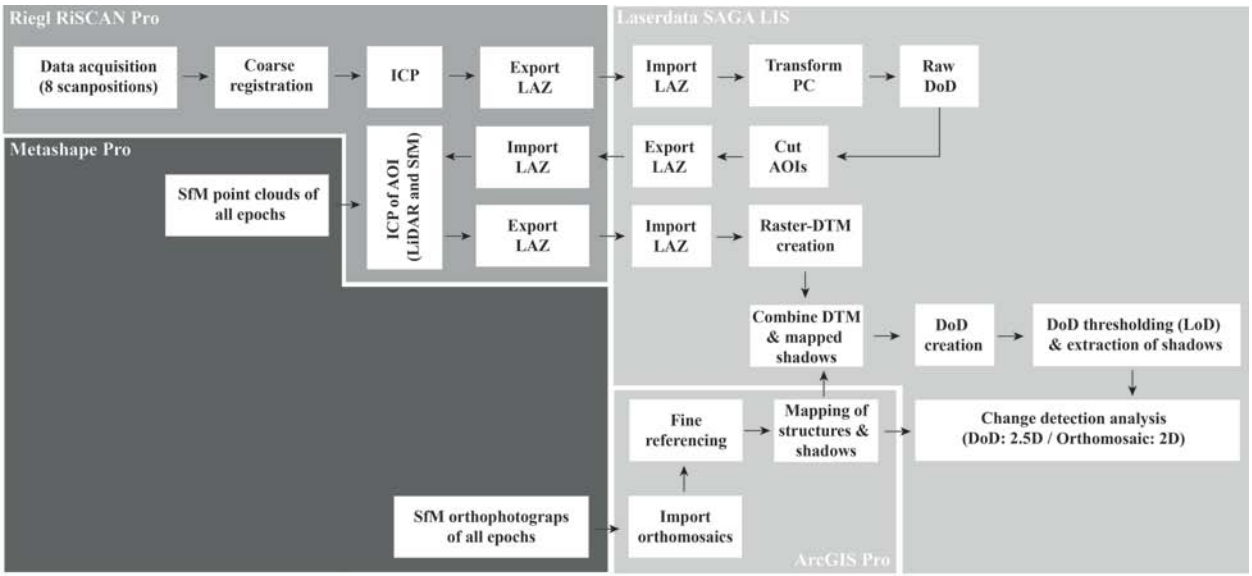

Fig. 4. Overall workflow of data processing of the TLS, terrestrial digital imagery and terrestrial historical data sets. The individual processing steps were shown for the corresponding software (Riegl RiSCAN PRO, Metashape Pro, Laserdata SAGA LIS, ArcGIS Pro).

Since it was not possible to detect CPs on the steep rock faces, we used stable areas to calculate the level of detection. The standard deviations of differences between two DTMs can be used for the calculation of the error for the resulting DoD using a simple Gaussian error propagation (i.e. Lane et al. 2003)

$$\delta_{diff} = \sqrt{\delta_1^2 + \delta_2^2} \quad (1)$$

with δ_{diff} representing the standard deviation of the stable areas. Under the assumption that errors are statistically independent, the *t*-value of each DoD-cell can be calculated with

$$t = \frac{z_1 - z_2}{\delta_{diff}} \quad (2)$$

and be compared to a critical *t*-value (*tcrit*). Here, we used a confidence interval of 87%, corresponding to a *tcrit* of |1.5|. All $|t|>1.5$ to be considered statistically significant surface changes. The resulting LoD (Table 7) is then calculated according to Lane et al. (2003)

$$LoD = tcrit \sqrt{\delta_1^2 + \delta_2^2} \quad (3)$$

Due to the different acquisition configurations the individual DTMs are subject to uncertainties of different magnitudes. To exclude the areas erroneously declared as process areas, a clump filter was used (Olaya 2004, SAGA LIS). The clump filter detects the neighbourhood pixels with similar values and groups them. Depending on the settings of the threshold values, the clumps are then formed and all other pixels (lone pixels and small pixel clumps) can be changed to no-data (eliminated). The further analyses are only based on clumps of a specific defined extend (minimum number of cells, defined as a clump: 120).

After these steps, volume changes of rockfall areas can be determined by subtracting the individual DTMs from each other. For the calculation of surface changes, all grid cells with negative values within the rock fall areas were first summed up and then multiplied by the square cell size.

$$V = \sum DoD * L^2 \quad (4)$$

Using the sum of the negative cell values $\sum DoD$ the net volumetric sediment change *V* can be calculated with the raster cell size *L*.

3.3.2 Mapping of shadows and topographic changes in terrestrial historical photomosaics

The individual terrestrial historical datasets differ greatly in terms of radiometric and spatial resolution but also in

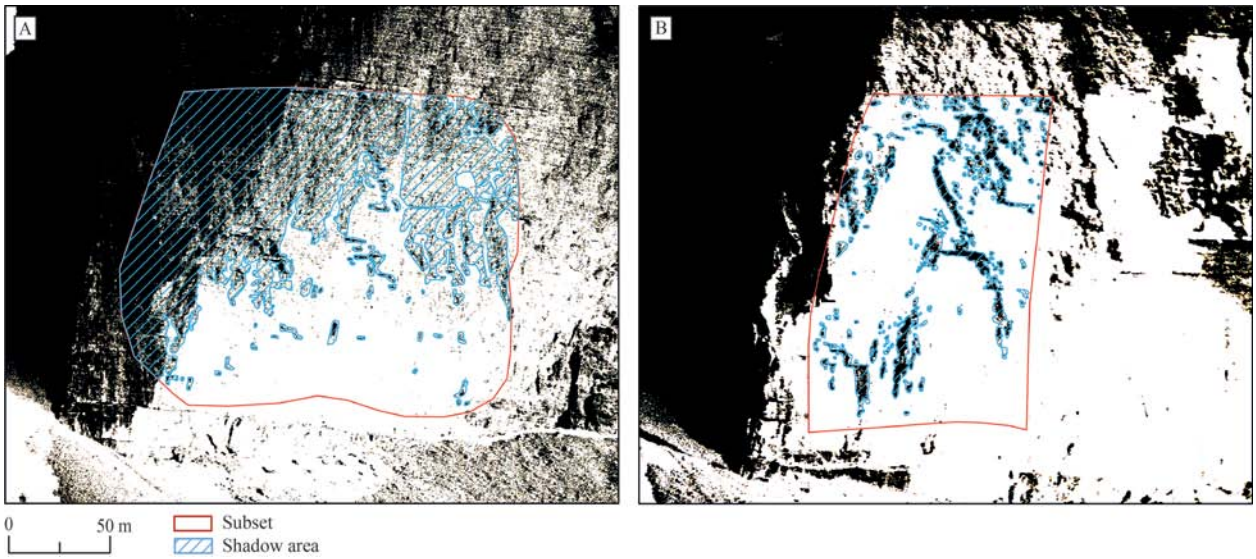

Fig. 5. Masked shadow areas of the historical images for the *Cima Grande* **(A)** and *Cima Ovest* **(B)**. The contrast value of the historical images was set to 100%. The two areas "subset", highlighted with red polygons, were investigated in more detail.

terms of entropy (exposure, contrast, etc.) and quality (physical degradation of images). As SfM is very sensitive to contrast changes in adjacent pixels, shadows can produce errors in the derived DTMs (especially in *z*-dimension). To exclude all shadowed areas from the DoD analysis, the contrast value for the historical photos was set to the maximum value (ArcGIS Pro). This facilitated the identification of shadow areas and their exclusion (reclassification tool in SAGA LIS) (Fig. 5).

To verify the derived surface changes, we tried to map major structures e.g. ridges or rock shelters in every single epoch. Figure 6 shows an exemplary mapping of these structures on the rock face. The 2D mapping was carried out in ArcGIS Pro for changes in the rock face in all epochs.

4 Results

The following chapter shows the results of TLS data processing before chapter 4.2 focuses on the results of the DTM generation from the historical photo data. The results of the change detection analysis are shown in chapter 4.3.

4.1 DTM generation from TLS data

The single scans from eight different scan positions resulted in a final 3D point cloud with approx. 56 million points with an average point density of 20.16 points/m². The co-registration of the single scans yielded a mean StD of 0.022 m (range: 0.015–0.038 m).

4.2 SfM-MVS processing of historical images

Table 6 shows the main parameters of SfM processing of the historical images for both AOIs (*Cima Grande, Cima Ovest*). The point densities, the number of points and the resulting photomosaic resolution for the year 1970 are remarkable. Rectified photomosaics were calculated for the historical data of 1970 and also for 1914 as well as for the high-resolution data of 2018 (Fig. 7). Due to low photo quality the calculation of tie-points was not possible for the years 1902 and 1930 and no DTM or rectified photomosaic could be created for this period. Although point clouds could be calculated for the 1914 data, they were excluded from further analysis because of extreme distortions, which could not be minimized despite various camera parameter settings. For this data, only 2D analysis on the photomosaics was conducted. Although the 1964/65 and 1979 photographs allowed the calculation of photomosaics, we refrained from further use of these data (change detection analysis) due to the extreme distortions that could not be corrected even by additional georeferencing operations.

4.3 Change detection analysis

4.3.1 2D-mapping of rock wall structures

Based on generated photomosaics, Figure 8 shows examples of rock areas where major changes could be mapped for the respective time periods. Looking at the 2018 mapping, it is noticeable that many of the structures that were visible in 1914 and 1970 (Fig. 8), such as outcrops,

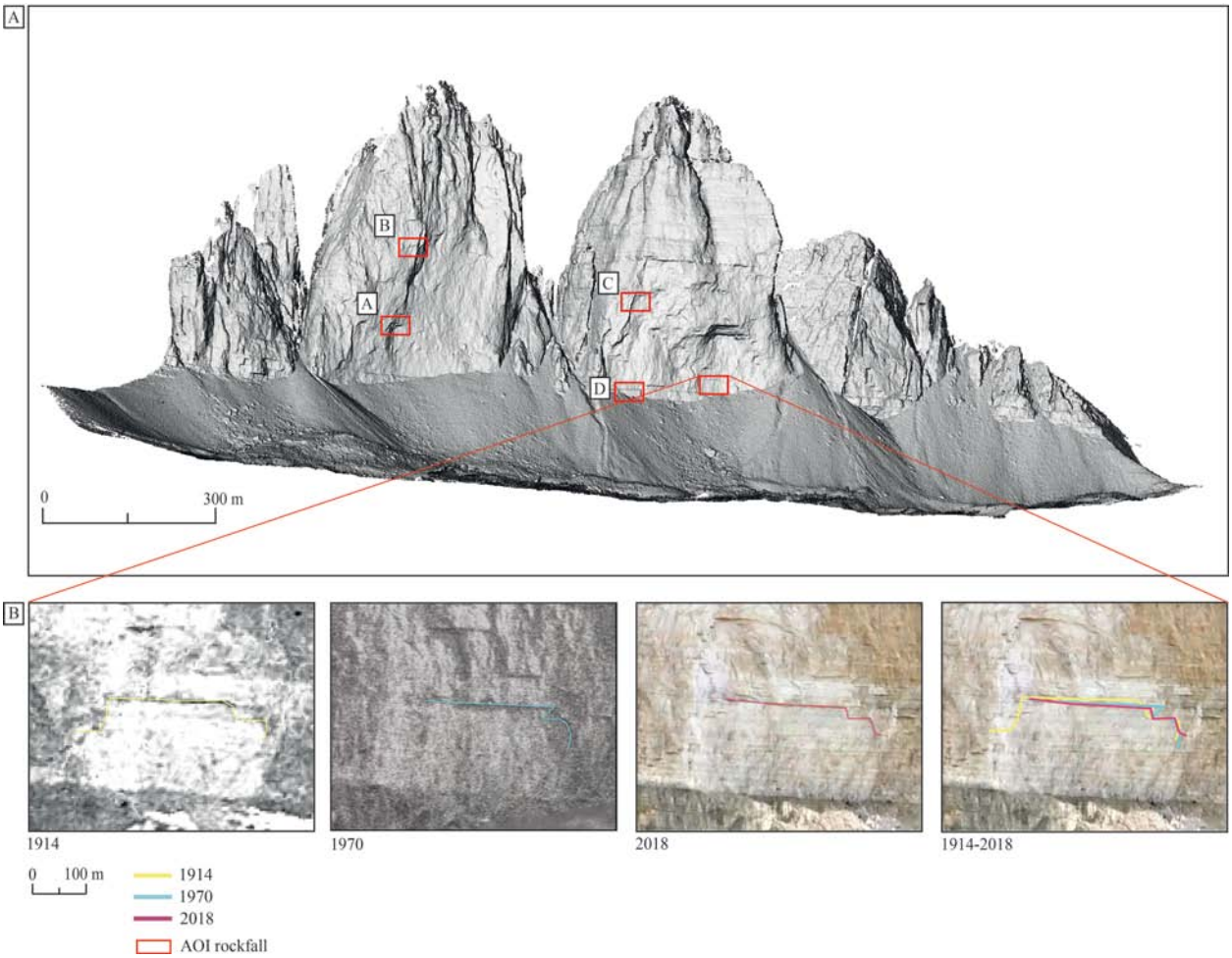

Fig. 6. (A). Hillshade of the entire *Tre Cime di Lavaredo*. The red squares A, B, C and D show the locations of the rockfall AOIs (discussed and shown in more detail later on in Chapter 4.3.1. and Fig. 8). For the areas in **(A)** and **(C)**, a further change detection analysis was carried out (see Chapter 4.3.2). **(B)**. Exemplary mapping of the structures in the rock face for all time slices used. View in south direction.

ridges, etc., mostly along the stratigraphy of the banked limestones, have changed, in some cases significantly, or were no longer present (Fig. 8A, C). The mapped area on the rock face of *Cima Ovest* (based on the 2018 photo) in Figure 8C, where there is a change in the rock face based on the photo verification, has an area of 21,870.51 m². The second mapped area on its rock face has an area of 64,269.12 m² (Fig. 8D). Based on the two-dimensional mapping of visible changes, DoD analysis were then used to quantify these changes (see Chapter 4.3.2).

4.3.2 Surface changes between 1970–2018 (DoD analysis)

The generated CPs from the TLS point cloud were successfully used to register the entire rock faces and the selected process areas. Due to the previously mentioned limitations regarding the quality of certain historical image sets, it was not possible to calculate DoD for all areas. Therefore, the change detection analysis was conducted on two specific process areas (see Fig. 8A and C in Chapter 4.3.1) for the observation period 1970–2018. The accuracies of the point cloud co-registrations and corresponding LoDs are summarised in Table 7 for both rock faces.

Despite the exclusion of the shadows (see Fig. 5) and areas with cell-changes below the respective LoD, we recognized some small fragmented zones of surface changes, which could not be verified by visual inspections (comparison of the respective orthomosaics) (Fig. 9). Although the areas of the individual changes are very small, they risk distorting the change values and therefore were excluded with the clump filter.

The filtered DoD for the *Cima Grande* clearly shows that a compact rock area broke out of the rock face

Table 6. Results of archival (1914, 1970) and 2018 image data processing.

Data	1914	1970		2018
	***Cima Grande* and *Cima Ovest* combined**	***Cima Grande***	***Cima Ovest***	***Cima Grande* and *Cima Ovest* combined**
Number of images	2	42	42	118
Mean sensor-object distance	2,700 m	1,520 m	1,690 m	1,610 m
Number of CPs	8	7	8	12
Control points RMSE (*x, y, z*)	4.6 m	0.32 m	0.47 m	0.19 m
Tie-points unfiltered [count]	187	18,330	18,424	87,293
Tie-points filtered [count]	–	14,997	15,314	67,686
RMS reprojection error	0.08 m	0.28 m	0.33 m	0.21 m
Max. reprojection error	0.19 m	0.87 m	1.10 m	0.62 m
Point cloud [count]	213,286	655,885	2,941,098	26,965,809
Mean point cloud density	0.2 p/m²	1.2 p/m²	3.9 p/m²	7.43 p/m²
Photomosaic resolution	51 cm	29.3 cm	14.3 cm	18.2 cm

Table 7. Results of the ICP adjustment between the LiDAR (2018) and archival image data (1970) as well as the DoD analysis for the stable areas. The LoD was set to a confidence interval of 87%. "Subset" refers to the area shown in Figures 5 and 9.

DTM	ICPRMSE [m]		Stable area DoD [m]			
	Rockface	Subset	Min	Max	StD	LoD
Cima Grande	0.89	0.4263	–1.9160	2.5654	0.6106	0.9159
Cima Ovest	1.08	0.5153	–2.5259	2.1147	0.5752	0.8628

(Fig. 10A). This can be verified by a visual comparison of the photomosaics from 1970 and 2018 (Fig. 10C and D) as well as by the swath profile (bandwidth 2 m) shown in Figure 10B. Some horizontal overhangs are clearly visible in the 1970 historical image (Fig. 10C), while the 2018 photomosaics no longer show this structure. Our assumption that major geomorphological changes occurred between 1970 and 2018 in this area of the rock face could be confirmed by quantitative analysis of the DoD 1970–2018 which yielded a volumetric change of -101.28 m³ and an overall process area of 34.42 m².

Figure 11 shows the filtered DoD of the AOI on the rock face *Cima Ovest*. It is clearly visible that a large contiguous area broke out of the rock face. A comparison between the 1970 and the 2018 images confirmed the results of the DoD analysis. The outcropping area becomes evident by the brighter colour of the rock (Fig. 11C) which points towards a lower stage of weathering due to lower/shorter exposure to rain and solar radiation. Compared to the previously described process area, the area of *Cima Ovest* shows a much wider extent of 474.74 m² and higher negative volume change of -1,872.87 m³.

5 Discussion

5.1 Data collection, photo quality and data processing

Overall, our expectation that a large number of photos could be collected from such a well-known mountain massif as the *Tre Cime di Lavaredo* was confirmed with a total of 270 photos from 1902. Despite the large number of historical photos, only a small portion of 42 photos (15.56%) could be used for quantitative 3D-analysis (change detection). We see the main reasons for this in (i) the lack of image pairs (stereo-images), (ii) poor image quality or varying image qualities in stereo-pairs and (iii) difficulties in determining the exact recording date (year). Figure 12 shows some examples of collected historical photos which could not be used for processing and further analysis due to the previously mentioned requirements.

Some image sets (e.g. 1914) enabled a SfM-MVS based surface reconstruction, but the respective DEMs could not be used for quantitative analysis. Reasons therefore are large geometric distortions which cause high errors in the *z*-dimension of the point clouds and

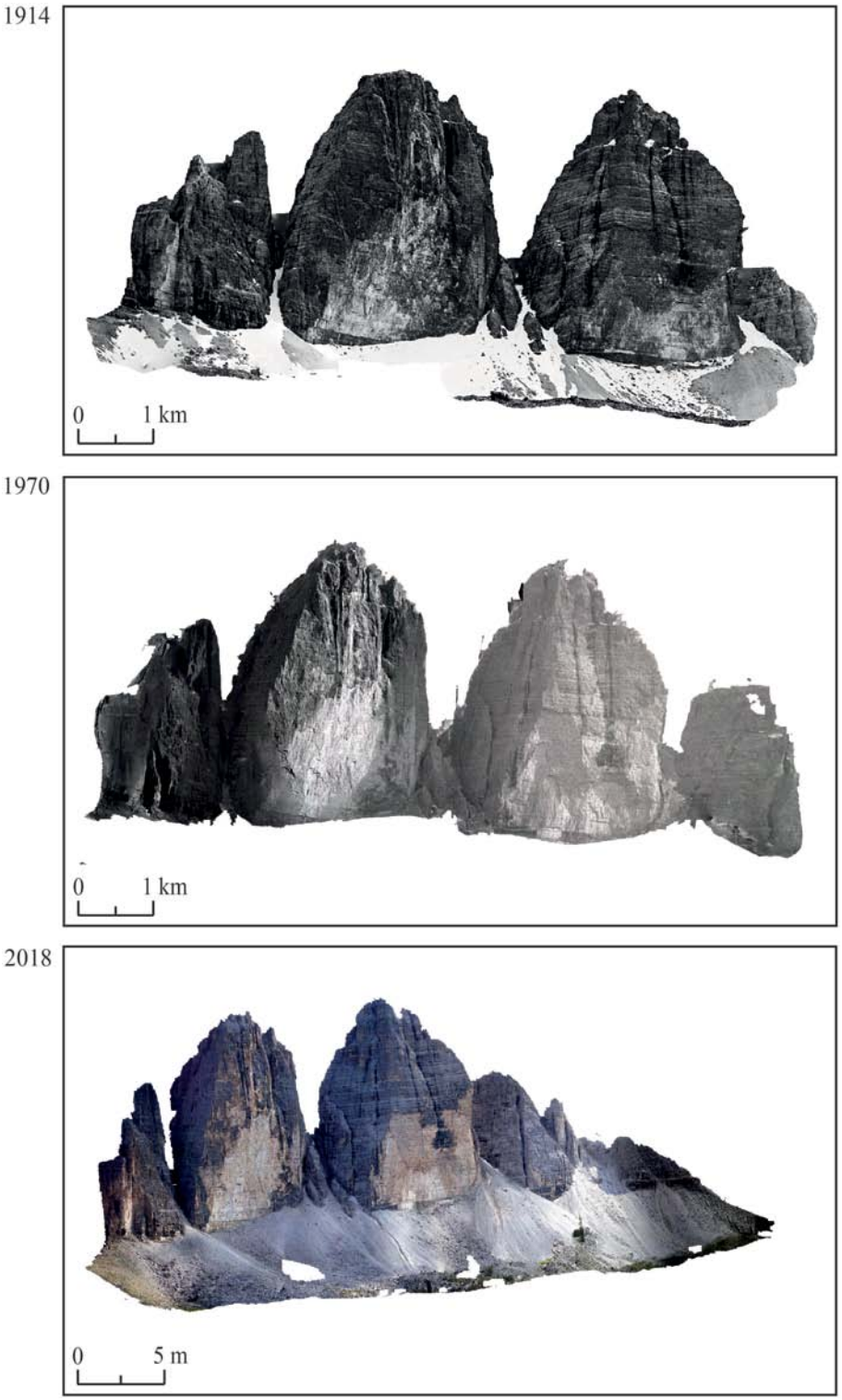

Fig. 7. Rectified photomosaics of the respective time slices 1914, 1970 and 2018. View in south direction.

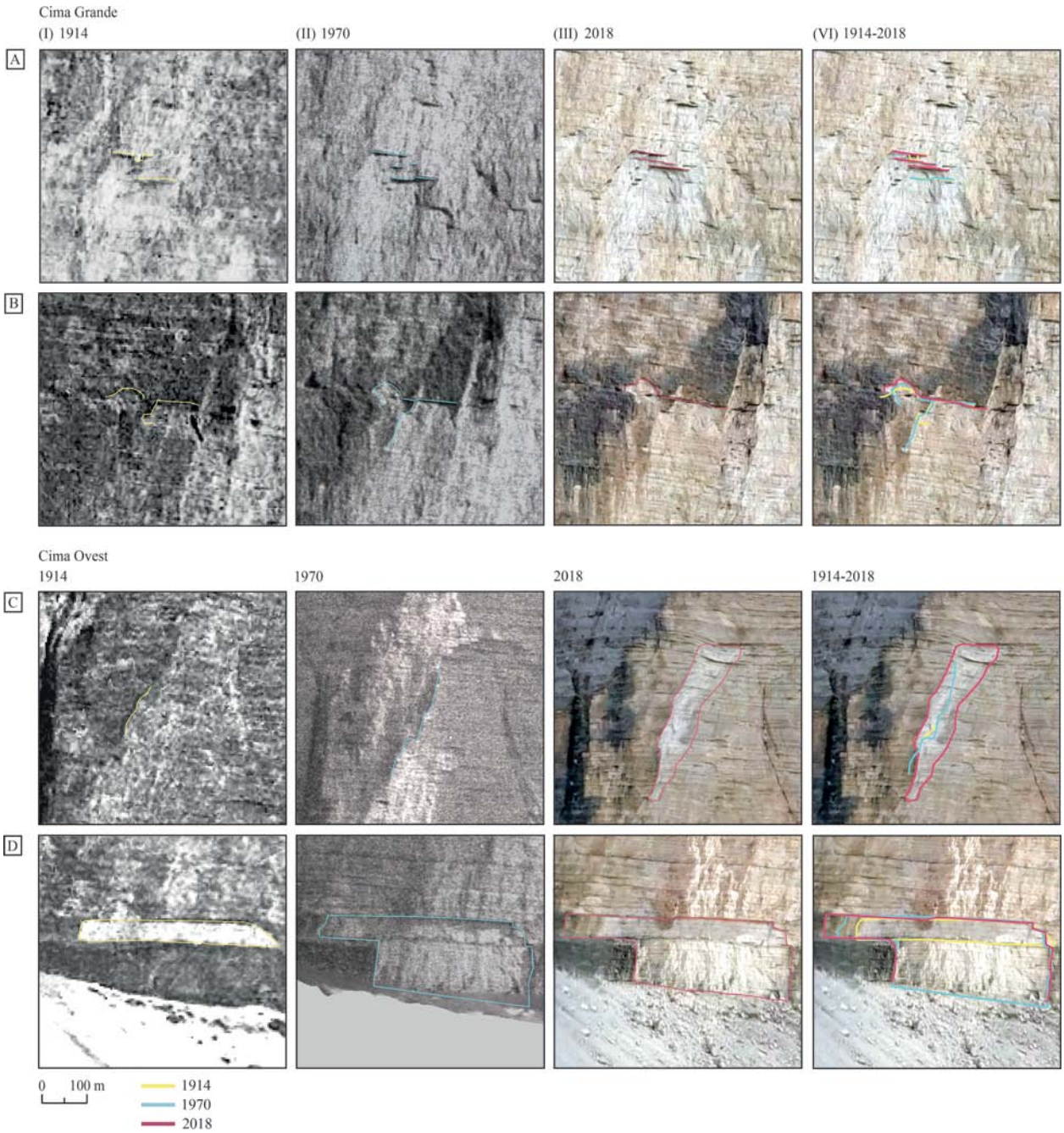

Fig. 8. 2D mapping of structures in the rock walls based on the historic images for the years 1914 (I), 1970 (II), the current dataset from 2018 (III) and surface changes (IV). **(A)**–**(D)** represent the areas shown in Figure 6 A. For the areas in **(A)** and **(C)**, a further change detection analysis was carried out (see Chapter 4.3.2).

respective DEMs. Despite the implementation of various processing strategies and parameters (SfM-MVS), these errors could not be minimized further. Therefore, we refrained from the use of the 3D point cloud (and DEM) of this data set and only used the photomosaic for two-dimensional analysis (mapping of structures and process areas, see Chapter 4.3.1).

Other data, such as the 1965 images showed unsuitable camera poses, overlaps or overexposure. Consequently, no tie-points can be found on the bright unweathered rock

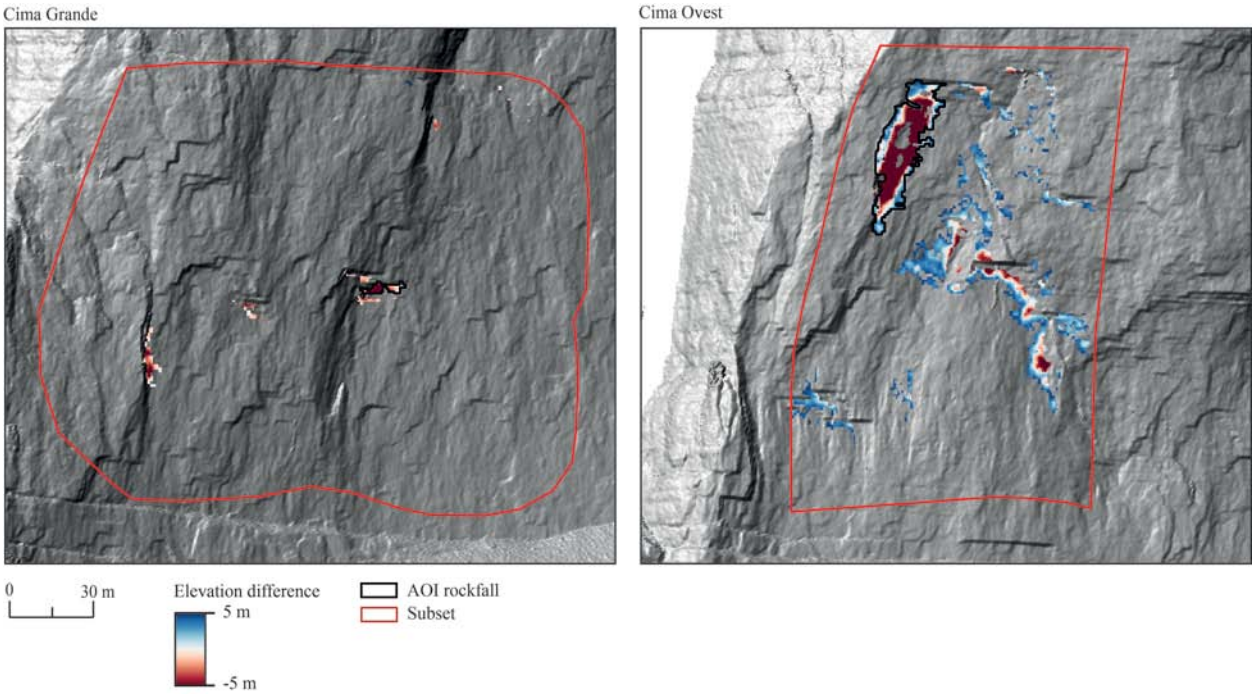

Fig. 9. DoD with applied LoD (see Table 7) and excluded shadow areas of the corresponding time epoch (1970–2018) for the two areas of the rock faces *Cima Grande* and *Cima Ovest*. The two "AOI rockfall" areas are the same as those shown in Figure 8 A and C. "Subset" represents the area that is also marked as a red polygon in Figure 5. View in south direction.

areas, as for the period of 1902–1930. The 1964/1965 and 1979 images could be processed into point clouds but the DEMs showed large geometric distortions which can be attributed to insufficient camera angles and low input quality of the images. This led to only a few tie-points as the software was not able to reconstruct the respective lens distortion parameters correctly and to calculate the appropriate camera model. This is consistent with Gomez et al. (2015) and Bakker & Lane (2017) who both point out the importance of image texture (entropy) for the bundle adjustment and feature extractions (tie-points) in the SfM processing. Aguilar et al. (2013) showed that the differences in the accuracy of a photogrammetric DTM depend significantly on the quality of bundle adjustment performances (generation of tie-points and reconstruction of camera positions based on the cameras exterior orientation parameters) and is therefore ultimately determined by the calculated camera model (e.g. Brown's 8-parameter model; Brown 1971). Relatively low image counts and image overlaps (such as in the historical data of 1902–1930, 1964/65 and 1979) can be accounted as major characteristics which contribute to difficulties in the SfM-based reconstruction of surfaces (Haas et al. 2016) and camera positions.

Image quality, especially resolution, plays another important role in image-based surface reconstruction as it determines the ability to detect terrain structures and to accurately define the location of CPs. This influences the accuracy and resolution of the final SfM-MVS product (Chirico et al. 2020). In addition to the general ability to accurately extract tie-points for feature matching, Mosbrucker et al. (2017) identified resolution or "ground sample distance" (GSD) as one of the most important factors in the quality of SfM-MVS derived products which is confirmed by the present study (photomosaic resolutions: 1914: 51 cm; 1964/65: 29.3 cm; 1970: 14.3 cm; 2018: 18.2 cm).

The discrepancies between the RMSE of the first (0.89 m for *Cima Grande* and 1.08 m for *Cima Ovest)* and the second registration steps (0.4263 m for *Cima Grande* and 0.5153 m for *Cima Ovest)* show the importance of further local co-registration processes (ICP adjustments) to minimize systematic errors in the respective DTMs. This consequently minimizes change detection thresholds and reduces noise in the DoD which leads to a more reliable detection of surface changes. This is in concordance with Stark et al. (2022) who have shown that a subsequent co-registration process of point clouds, first carried out on a wider area (e.g. rock face or catchment area) and second on a smaller process area (e.g. rockfall area, specific slope), minimizes systematic errors significantly.

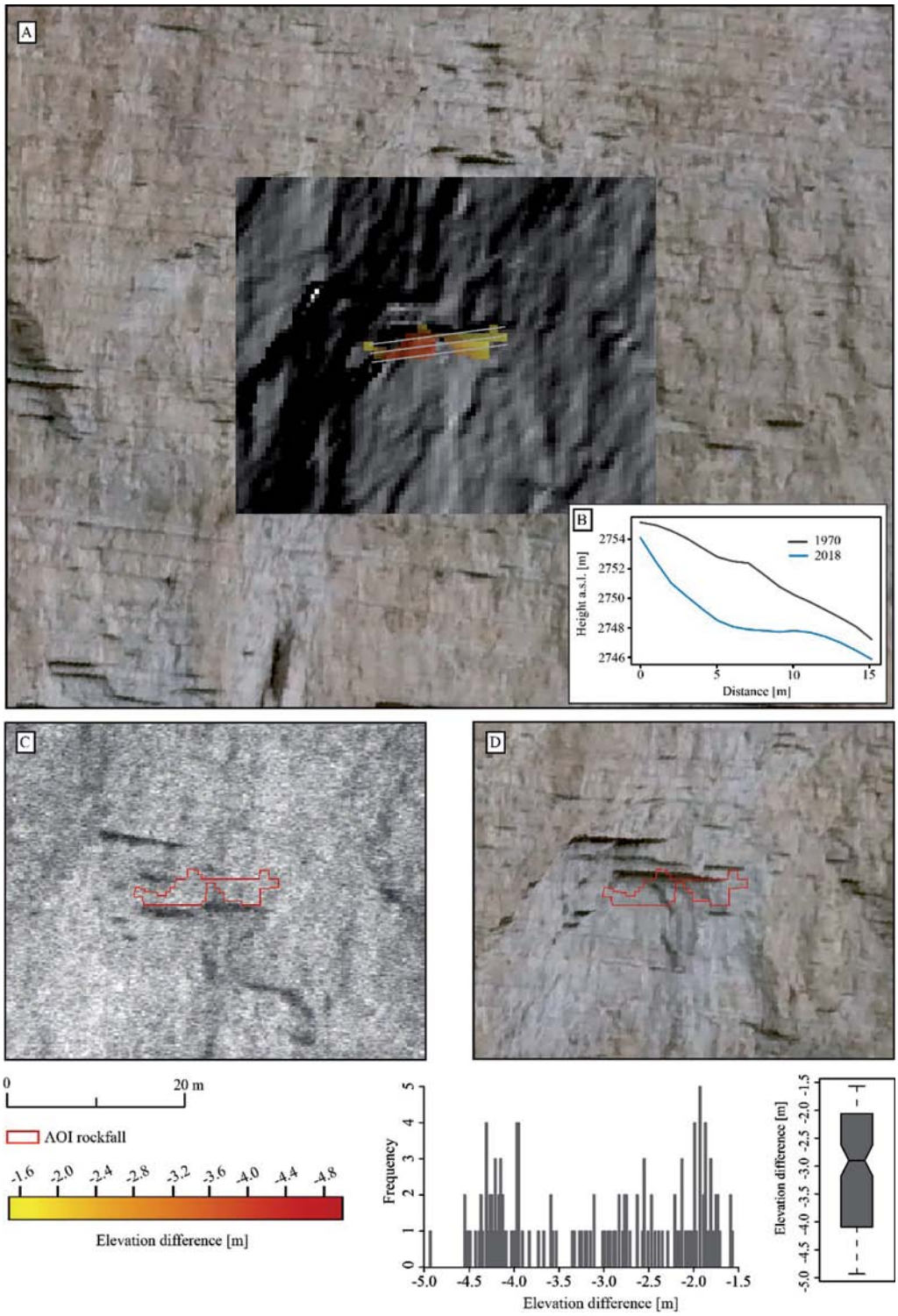

Fig. 10. Filtered DoD for the observation period 1970 to 2018 for the *Cima Grande* with a terrestrial digital image of 2018 and a hillshade **(A)**. This area is marked with the black polygon (AOI rockfall) in Figure 9 and correspond to the AOI **(A)** in Fig. 6. **(B)** shows a swath profile (2 m) for the respective data set. **(C)** and **(D)** show the erosion area based on the historical photo and the terrestrial digital image taken in 2018. View in south direction.

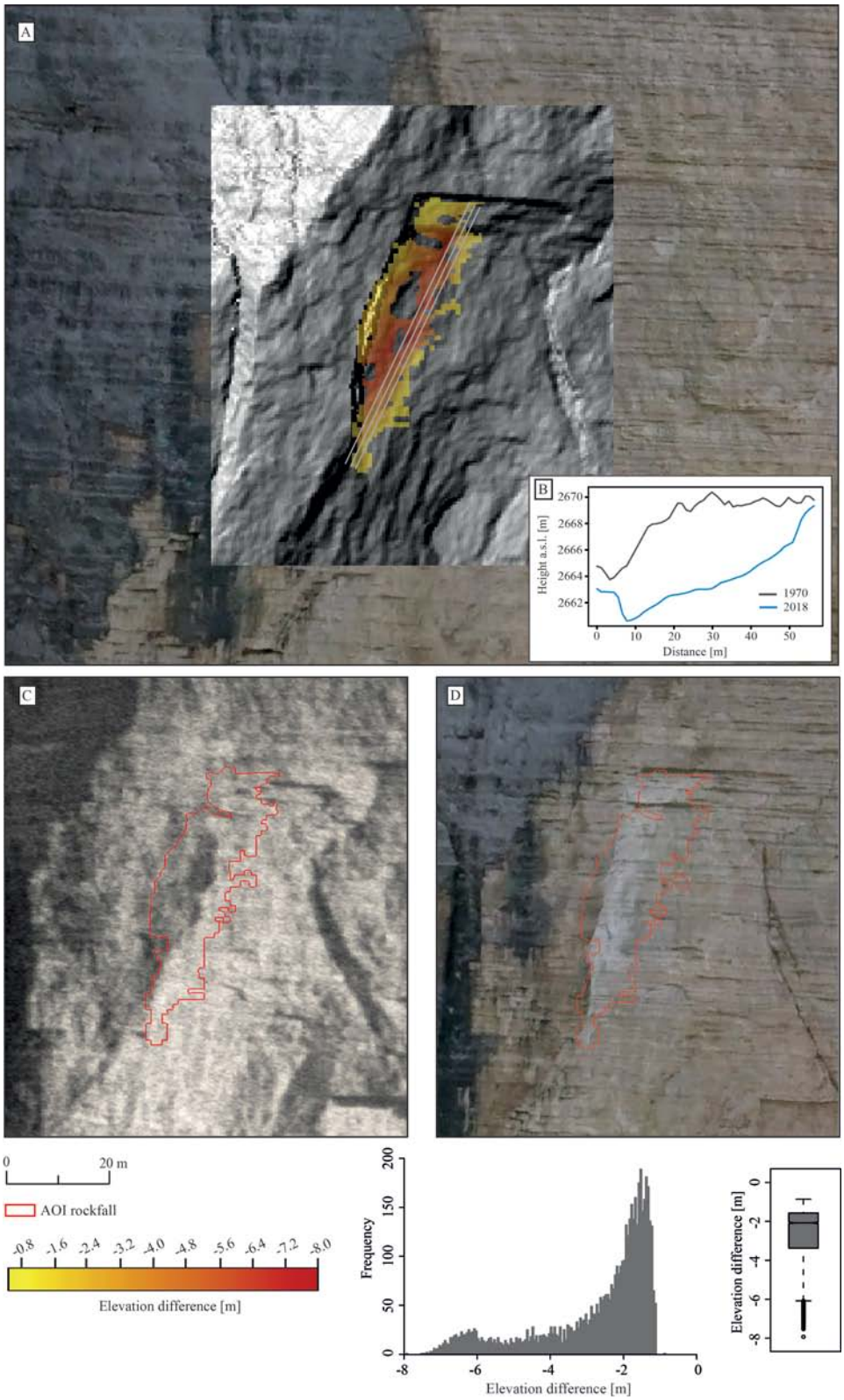

Fig. 11. Filtered DoD for the observation period 1970 to 2018 for the *Cima Ovest* with a terrestrial digital image of 2018 and a hillshade **(A)**. This area is marked with the black polygon (AOI rockfall) in Figure 9 and correspond to the AOI **(C)** in Figure 6. **(B)** shows a swath profile (2 m) for the respective data set. **(C)** and **(D)** show the erosion area based on the historical photo and the terrestrial digital image taken in 2018. View in south direction.

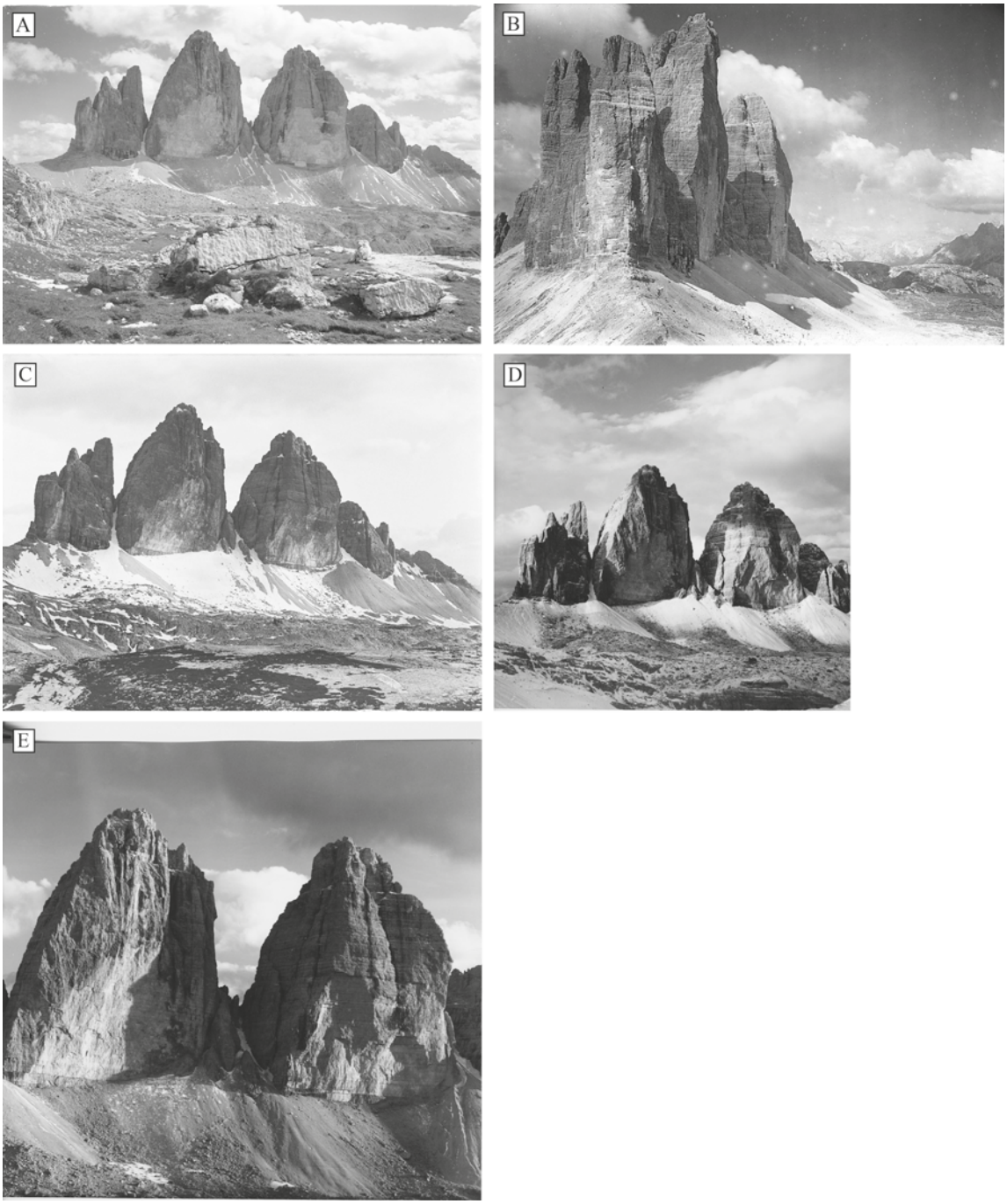

Fig. 12. An overview of the images those are not suitable for SfM-MVS processing due to different quality insufficiencies. **(A)**: The photo cannot be used for further processing due to its perspective. The other images from this data set have a comparable perspective. The date of the photo is between 1902–1930. Information about the exact date of taking the photo is not available (source: Amt für Film und Medien, Bozen, Südtirol, Italy). **(B)**: Due to contamination of the photo, it is also not processable. The perspective does not allow this either. The date when the photo was taken is between 1902 and 1939. More precise information about the exact date when the photo was taken is not available (source: Amt für Film und Medien, Bozen, Südtirol, Italy). **(C)**: This image has a different perspective between camera and object. It consists of a second photo. The photo was taken in 1914 (source: Universalarchiv der Deutschen Fotothek für Kunst- und Kulturgeschichte, Dresden, Germany). **(D)** and **(E)**: The rock faces of the two images have too many shadow areas which make point cloud processing impossible. The photo in **(D)** was taken in 1964 and the photo in **(E)** in 1979 (source: both Fotohaus Heimhuber (private archive)).

Unfortunately, the question of whether historical images are suitable for surface reconstruction of steep rock faces cannot be answered in general on the basis of specific parameters such as resolution, number of exposures or object-sensor-distance. Due to the varying qualities of the individual data sets, careful examination and preparation of the data is essential to answer the question of suitability. This includes, above all, constant controls within the individual processing steps.

5.2 Change detection

Based on the present workflow, the volume changes for the period 1970–2018 were successfully quantified. However, visual validations of the DoD revealed some outliers and incorrectly calculated surfaces due to differently pronounced shadows in the single images. This problem had been expected in the north walls of the *Tre Cime di Lavaredo*, as light and shadow in the area of the north walls change extremely depending on the time of the year and day. This led to variable lighting conditions in the images and problems in the SfM-MVS based surface reconstruction of certain data. The automatic filtering of the shadow areas led to an exclusion of these areas from the DoD and prevented erroneously reconstructed surfaces due to shadows from being included in the quantification of the volume changes. Unfortunately, this also led to an exclusion of shadow-affected areas for which smaller surface changes could be visually validated. Furthermore, the LoD led to the exclusion of additional areas for which surface changes could be verified on basis of the 2D-analysis (mapping of rock structures).

Finally, our analysis revealed two bigger rockfalls which caused extensive volumetric changes of -101.28 m³ for *Cima Grande* and -1,872.87 m³ for *Cima Ovest* between 1970 and 2018. Due to the filtering and the consideration of the LoD these volumes must be seen as minimum values. For example, the 1970–2018 DoD for the *Cima Ovest* shows a rockfall area of 474.74 m² (Fig. 11), whereas the respective 2D mapped measures 21,870.51 m². From the ratio, the filtered DoD corresponds to an area of 2.17% of the total process area.

Apart from the methodological limitations and possible options for further studies, our work has shown that the *Tre Cime di Lavaredo* represent an area characterized by the occurrence of large rockfalls. This fits well with reported rockfalls on these rock walls, but also to other studies from the Dolomites. Up to now almost all studies analysed rockfalls by means of TLS and SfM-MVS (high-resolution digital images or aerial images), but they did not use historical terrestrial images. Viero et al. (2013) investigated e.g. a bigger rockfall at the *Cima Uno* from 2007, which is also located in the Sesto Dolomites near *Tre Cime di Lavaredo*, where 40,000 m³ of dolomitic rock collapsed. Also Haas et al. (2012) quantified the volume of a rockfall in the Dolomites (Val di Funes) in 2003 with 10,373 m³ and an area of 577 m². This area of detachment fits also well with that of *Cime Ovest* with 474.74 m².

6 Conclusion

Apart from the present study, no other study has used historical terrestrial photographs to reconstruct rockwall surface. The recent state of research provided a good database for short- to mid-term analysis, but long-term analyses (several decades) are lacking. We aimed to bridge this gap with the present study and to provide more insights in the opportunities and challenges of SfM-based surface reconstruction on historical terrestrial images.

Based on the useable historical terrestrial images and recent TLS data we were able to show that point clouds and high-resolution DTMs can be generated and that the detection and quantification of surface changes of rockfalls are possible over a larger period (1970–2018). But our work also showed that processing historical terrestrial photos requires a lot of effort to reduce inaccuracies as best as possible and that despite the great effort in processing uncertainties remain. These relatively high inaccuracies and the low data availability, which is suitable for 3D reconstructions, limit the validity of the study concerning the change of rockfall dynamics in alpine areas due to climate change. For the analysis of e.g. changing frequency-magnitude relations, photos back to the early 20th century with a high temporal resolution would be necessary. Nevertheless, the present study showed that changes in the rock faces can also be recorded based on two-dimensional mappings and those changes in rockfall activity could be analysed. Unfortunately, to derive a rectified orthomosaic a photogrammetric workflow has to be applied, which limits the 2D-approach to historical data with a minimum of two overlapping images from different perspectives.

The present study also showed, that the use of historical terrestrial images is challenging in many ways. The search for historical terrestrial photographs shows that public and private archives can provide a large number of images, but that this search is time-consuming. Surprisingly, the photos were available in very different qualities and only a small fraction of the images were available as at least stereo-pairs. Therefore, we recommend extending the investigations to private photo archives to increase the number of images that can be used for 3D surface reconstructions and quantitative analysis. Searches in private collections should additionally be publicized through public appeals (on television or in print media), and data should be supplemented, e.g., through citizen science approaches.

Future research should evaluate the potential of monoplotting tools which allow two-dimensional mapping of visible process areas. The mapped changes could then be used to estimate volumes based on current high-resolution elevation models (LiDAR), as shown for example by Guerin et al. (2020b) in the Mont Blanc Massif for historical mapping. This would then enable an in-depth analysis of system changes over larger periods (e.g., due to climate change). But initially, errors in the DTMs must be reduced to optimise the spatial resolution. For monoplotting tools, inaccuracies must be minimised. This would result in an improvement of temporal resolution.

Data availability: The data used in this study are accessible upon request by contacting Kerstin Wegner (kwegner@ku.de).

Author contributions: KW, MS, FH and MB conceptualized the idea of the study. KW and MS collected the terrestrial laser scanning data of the *Tre Cime di Lavaredo*. KW conducted the archival research. KW and MS processed the data. KW analysed the data. MS, FH and MB supervised the analyses. KW wrote the draft of the manuscript with discussions and improvements from all co-authors.

Competing interests: The authors declare that they have no conflict of interest.

Acknowledgements: We greatly thank the archives (Universalarchiv der Deutschen Fotothek für Kunst- und Kulturgeschichte, Dresden, Germany, Amt für Film und Medien in Bozen, Südtirol, Italy) and Fotohaus Heimhuber (private archive) for providing the historical data sets. We also acknowledge the help during field work by the student assistant Daniel Fischer.

Financial support: The open access publication of this article was funded by the Deutsche Forschungsgemeinschaft (DFG, German Research Foundation) – Projektnummer 512640851. This research received no other external funding.

References

Abellán, A., Vilaplana, J. M., Calvet, J., García-Sellés, D., & Asensio, E. (2011). Rockfall monitoring by Terrestrial Laser Scanning – case study of the basaltic rock face at Castellfollit de la Roca (Catalonia, Spain). *Natural Hazards and Earth System Sciences, 11*(3), 829–841. https://doi.org/10.5194/nhess-11-829-2011

Aber, J. S., Marzolff, I., Ries, J. B., & Aber, S. E. W. (2019). *Small-Format Aerial Photography and UAS imagery. Principles, Techniques, and Geoscience Applications*. Amsterdam: Elsevier; https://doi.org/10.1016/C2016-0-03506-4

Agisoft LLC (2019). *Agisoft metashape user manuals, Professional edition*. Retrieved from https://www.agisoft.com/downloads/user-manuals/

Agüera-Vega, F., Carvajal-Ramírez, F., & Martínez-Carricondo, P. (2017). Assessment of photogrammetric mapping accuracy based on variation ground control points number using unmanned aerial vehicle. *Measurement, 98*, 221–227. https://doi.org/10.1016/j.measurement.2016.12.002

Aguilar, M. A., Aguilar, F. J., Fernández, I., & Mills, J. P. (2013). Accuracy assessment of commercial self-calibrating bundle adjustment routines applied to archival aerial photography. *The Photogrammetric Record, 28*(141), 96–114. https://doi.org/10.1111/j.1477-9730.2012.00704.x

Altmann, M., Piermattei, L., Haas, F., Heckmann, T., Fleischer, F., Rom, J., … Becht, M. (2020). Long-term changes of morphodynamics on Little Ice Age lateral moraines and the resulting sediment transfer into mountain streams in the Upper Kauner Valley, Austria. *Water (Basel), 12*(12), 3375. https://doi.org/10.3390/w12123375

Autonome Provinz Bozen-Südtirol (2008). *Natura 2000 Managementplan. Naturpark Drei Zinnen*. Retrieved from http://www.provinz.bz.it/natur-umwelt/natur-raum/downloads/Bericht_MP_NP-DZ_dt.pdf

Bakker, M., & Lane, S. N. (2017). Archival photogrammetric analysis of river-floodplain systems using Structure from Motion (SfM) methods. *Earth Surface Processes and Landforms, 42*(8), 1274–1286. https://doi.org/10.1002/esp.4085

Benjamin, J., Rosser, N. J., & Brain, M. J. (2020). Emergent characteristics of rockfall inventories captured at a regional scale. *Earth Surface Processes and Landforms, 45*(12), 2773–2787. https://doi.org/10.1002/esp.4929

Bennett, G. L., Molnar, P., Eisenbeiss, H., & McArdell, B. W. (2012). Erosional power in the Swiss Alps: Characterization of slope failure in the Illgraben. *Earth Surface Processes and Landforms, 37*(15), 1627–1640. https://doi.org/10.1002/esp.3263

Betz, S., Croce, V., & Becht, M. (2019). Investigating morphodynamics on Little Ice Age lateral moraines in the Italian Alps using archival aerial photogrammetry and airborne LiDAR data. *Zeitschrift für Geomorphologie, 62*(3), 231–247. https://doi.org/10.1127/zfg/2019/0629

Brasington, J., Langham, J., & Rumsby, B. (2003). Methodological sensitivity of morphometric estimates of coarse fluvial sediment transport. *Geomorphology, 53*(3-4), 299–316. https://doi.org/10.1016/S0169-555X(02)00320-3

Brown, D. C. (1971). Close-range camera calibration. *Photogrammetric Engineering, 37*, 855–866.

Cabo, C., Sanz-Ablanedo, E., Roca-Pardiñas, J., & Ordóñez, C. (2021). Influence of the number and spatial distribution of ground control points in the accuracy of UAV-SfM DEMs: An approach based on generalized additive models. *IEEE Transactions on Geoscience and Remote Sensing, 59*(12), 10618–10627. https://doi.org/10.1109/TGRS.2021.3050693

Carrivick, J. L., Smith, M. W., & Quincey, D. J. (2016). *Structure from Motion in the Geosciences*. Chichester: Wiley. https://doi.org/10.1002/9781118895818

Casagli, N., Frodella, W., Morelli, S., Tofani, V., Ciampalini, A., Intrieri, E., … Lu, P. (2017). Spaceborne, UAV and ground-

based remote sensing techniques for landslide mapping, monitoring and early warning. *Geoenvironmental Disasters, 4*(1), 9. https://doi.org/10.1186/s40677-017-0073-1

Chirico, P., DeWitt, J., & Bergstresser, S. (2020). Evaluating elevation change thresholds between structure-from-motion DEMs derived from historical aerial photos and 3DEP LiDAR data. *Remote Sensing (Basel), 12*(10), 1625. https://doi.org/10.3390/rs12101625

Conrad, O., Bechtel, B., Bock, M., Dietrich, H., Fischer, E., Gerlitz, L., … Böhner, J. (2015). System for Automated Geoscientific Analyses (SAGA) v. 2.1.4. *Geoscientific Model Development, 8*(7), 1991–2007. https://doi.org/10.5194/gmd-8-1991-2015

Derrien, A., Peltier, A., Villeneuve, N., & Staudacher, T. (2020). The 2007 caldera collapse at Piton de la Fournaise: new insights from multi-temporal structure-from-motion. *Volcanica, 3*(1), 55–65. https://doi.org/10.30909/vol.03.01.5565

Eker, R., Aydın, A., & Hübl, J. (2018). Unmanned aerial vehicle (UAV)-based monitoring of a landslide: Gallenzerkogel landslide (Ybbs-Lower Austria) case study. *Environmental Monitoring and Assessment, 190*(1), 28. https://doi.org/10.1007/s10661-017-6402-8

Eltner, A., Kaiser, A., Castillo, C., Rock, G., Neugirg, F., & Abellán, A. (2016). Image-based surface reconstruction in geomorphometry – merits, limits and developments. *Earth Surface Dynamics, 4*(2), 359–389. https://doi.org/10.5194/esurf-4-359-2016

Fey, C., & Wichmann, V. (2017). Long-range terrestrial laser scanning for geomorphological change detection in alpine terrain – handling uncertainties. *Earth Surface Processes and Landforms, 42*(5), 789–802. https://doi.org/10.1002/esp.4022

Fleischer, F., Haas, F., Piermattei, L., Pfeiffer, M., Heckmann, T., Altmann, M., … Becht, M. (2021). Multi-decadal (1953–2017) rock glacier kinematics analysed by high-resolution topographic data in the upper Kaunertal, Austria. *The Cryosphere, 15*(12), 5345–5369. https://doi.org/10.5194/tc-15-5345-2021

Frattini, P., Crosta, G. B., & Agliardi, F. (2012). Rockfall characterization and modeling. In J. J. Clague & D. Stead (Eds.), *Landslides, Types, Mechanisms and Modeling* (pp. 267–281). Cambridge, UK: Cambridge University Press. https://doi.org/10.1017/CBO9780511740367.023

Gallach, X., Carcaillet, J., Ravanel, L., Deline, P., Ogier, C., Rossi, M., … Garcia-Sellés, D. (2020). Climatic and structural controls on Late-glacial and Holocene rockfall occurrence in high-elevated rock walls of the Mont Blanc massif (Western Alps). *Earth Surface Processes and Landforms, 45*(13), 3071–3091. https://doi.org/10.1002/esp.4952

Gallo, I. G., Martínez-Corbella, M., Sarro, R., Iovine, G., López-Vinielles, J., Hérnandez, M., … García-Davalillo, J. C. (2021). An integration of UAV-based photogrammetry and 3D modelling for rockfall hazard assessment: The Cárcavos case in 2018 (Spain). *Remote Sensing (Basel), 13*(17), 3450. https://doi.org/10.3390/rs13173450

Geissler, J., Mayer, C., Jubanski, J., Münzer, U., & Siegert, F. (2021). Analyzing glacier retreat and mass balances using aerial and UAV photogrammetry in the Ötztal Alps, Austria. *The Cryosphere, 15*(8), 3699–3717. https://doi.org/10.5194/tc-15-3699-2021

Gomez, C., Hayakawa, Y., & Obanawa, H. (2015). A study of Japanese landscapes using structure from motion derived DSMs and DEMs based on historical aerial photographs: New opportunities for vegetation monitoring and diachronic geomorphology. *Geomorphology, 242*, 11–20. https://doi.org/10.1016/j.geomorph.2015.02.021

Guerin, A., Stock, G. M., Radue, M. J., Jaboyedoff, M., Collins, B. D., Matasci, B., … Derron, M.-H. (2020a). Quantifying 40 years of rockfall activity in Yosemite Valley with historical Structure-from-Motion photogrammetry and terrestrial laser scanning. *Geomorphology, 356*, 107069. https://doi.org/10.1016/j.geomorph.2020.107069

Guerin, A., Ravanel, L., Matasci, B., Jaboyedoff, M., & Deline, P. (2020b). The three-stage rock failure dynamics of the Drus (Mont Blanc massif, France) since the June 2005 large event. *Scientific Reports, 10*(1), 17330. https://doi.org/10.1038/s41598-020-74162-1

Haas, F., Heckmann, T., Wichmann, V., & Becht, M. (2012). Runout analysis of a large rockfall in the Dolomites/Italian Alps using LIDAR derived particle sizes and shapes. *Earth Surface Processes and Landforms, 37*(13), 1444–1455. https://doi.org/10.1002/esp.3295

Haas, F., Hilger, L., Neugirg, F., Umstädter, K., Breitung, C., Fischer, P., … Becht, M. (2016). Quantification and analysis of geomorphic processes on a recultivated iron ore mine on the Italian island of Elba using long-term ground-based lidar and photogrammetric SfM data by a UAV. *Natural Hazards and Earth System Sciences, 16*(5), 1269–1288. https://doi.org/10.5194/nhess-16-1269-2016

Heckmann, T., Bimböse, M., Krautblatter, M., Haas, F., Becht, M., & Morche, D. (2012). From geotechnical analysis to quantification and modeling using LiDAR data: A study on rockfall in the Reintal catchment, Bavarian Alps, Germany. *Earth Surface Processes and Landforms, 37*(1), 119–133. https://doi.org/10.1002/esp.2250

Heiser, M., Scheidl, C., & Kaitna, R. (2017). Evaluation concepts to compare observed and simulated deposition areas of mass movements. *Computational Geosciences, 21*(3), 335–343. https://doi.org/10.1007/s10596-016-9609-9

Hemmelder, S., Marra, W., Markies, H., & De Jong, S. M. (2018). Monitoring river morphology & bank erosion using UAV imagery – A case study of the river Buëch, Hautes-Alpes, France. *International Journal of Applied Earth Observation and Geoinformation, 73*, 428–437. https://doi.org/10.1016/j.jag.2018.07.016

Hungr, O., & Evans, S. G. (1988). Engineering evaluation of fragmental rockfall hazards. *Proceedings of the 5th International Symposium on Landslides in Lausanne* (p. 685–690). Rotterdam: Balkema.

IPCC (2021). Climate Change 2021: The Physical Science Basis. Contribution of Working Group I to the Sixth Assessment Report of the Intergovernmental Panel on Climate Change. In V. Masson-Delmotte, A. Pirani, S. L. Connors, C. Péan, S. Berger, N. Caud, & B. Zhou (Eds.), Cambridge, UK: Cambridge University Press.

James, M. R., Robson, S., d'Oleire-Oltmanns, S., & Niethammer, U. (2017a). Optimising UAV topographic surveys pro-

cessed with structure-from-motion: Ground control quality, quantity and bundle adjustment. *Geomorphology, 280*, 51–66. https://doi.org/10.1016/j.geomorph.2016.11.021

James, M. R., Robson, S., & Smith, M. W. (2017b). 3-D uncertainty-based topographic change detection with structure-from-motion photogrammetry: Precision maps for ground control and directly georeferenced surveys. *Earth Surface Processes and Landforms, 42*(12), 1769–1788. https://doi.org/10.1002/esp.4125

James, M. R., Antoniazza, G., Robson, S., & Lane, S. N. (2020). Mitigating systematic error in topographic models for geomorphic change detection: Accuracy, precision and considerations beyond off-nadir imagery. *Earth Surface Processes and Landforms, 45*(10), 2251–2271. https://doi.org/10.1002/esp.4878

Jaud, M., Letortu, P., Théry, C., Grandjean, P., Costa, S., Maquaire, O., … Le Dantec, N. (2019). UAV survey of a coastal cliff face – selection of the best imaging angle. *Measurement, 139*, 10–20. https://doi.org/10.1016/j.measurement.2019.02.024

Krautblatter, M., & Dikau, R. (2007). Towards a uniform concept for the comparison and extrapolation of rockwall retreat and rockfall supply. *Geografiska Annaler. Series A. Physical Geography, 89*(1), 21–40. https://doi.org/10.1111/j.1468-0459.2007.00305.x

Lane, S. N., Westaway, R. M., & Hicks, D. M. (2003). Estimation of erosion and deposition volumes in a large, gravel-bed, braided river using synoptic remote sensing. *Earth Surface Processes and Landforms, 28*(3), 249–271. https://doi.org/10.1002/esp.483

Laporte-Fauret, Q., Marieu, V., Castelle, B., Michalet, R., Bujan, S., & Rosebery, D. (2019). Low-cost UAV for high-resolution and large-scale coastal dune change monitoring using photogrammetry. *Journal of Marine Science and Engineering, 7*(3), 63. https://doi.org/10.3390/jmse7030063

Legay, A., Magnin, F., & Ravanel, L. (2021). Rock temperature prior to failure: Analysis of 209 rockfall events in the Mont Blanc massif (Western European Alps). *Permafrost and Periglacial Processes, 32*(3), 520–536. https://doi.org/10.1002/ppp.2110

Linder, W. (2016). *Digital photogrammetry: a practical course*. Berlin: Springer; https://doi.org/10.1007/978-3-662-50463-5

Magnin, F., Josnin, J.-Y., Ravanel, L., Pergaud, J., Pohl, B., & Deline, P. (2017). Modelling rock wall permafrost degradation in the Mont Blanc massif from the LIA to the end of the 21st century. *The Cryosphere, 11*(4), 1813–1834. https://doi.org/10.5194/tc-11-1813-2017

Mayer, C., Gomes Pereira, L. M., & Kersten, T. P. (2018). A comprehensive workflow to process UAV images for the efficient production of accurate geo-information. *IX. National Conference on Cartography and Geodesy*, 1–8.

Mertes, J. R., Gulley, J. D., Benn, D. I., Thompson, S. S., & Nicholson, L. I. (2017). Using structure-from-motion to create glacier DEMs and orthoimagery from historical terrestrial and oblique aerial imagery. *Earth Surface Processes and Landforms, 42*(14), 2350–2364. https://doi.org/10.1002/esp.4188

Micheletti, N., Chandler, J. H., & Lane, S. N. (2015). Investigating the geomorphological potential of freely available and accessible structure-from-motion photogrammetry using a smartphone. *Earth Surface Processes and Landforms, 40*(4), 473–486. https://doi.org/10.1002/esp.3648

Mosbrucker, A. R., Major, J. J., Spicer, K. R., & Pitlick, J. (2017). Camera system considerations for geomorphic applications of SfM photogrammetry. *Earth Surface Processes and Landforms, 42*(6), 969–986. https://doi.org/10.1002/esp.4066

Müller, J., Gärtner-Roer, I., Thee, P., & Ginzler, C. (2014). Accuracy assessment of airborne photogrammetrically derived high-resolution digital elevation models in a high mountain environment. *ISPRS Journal of Photogrammetry and Remote Sensing, 98*, 58–69. https://doi.org/10.1016/j.isprsjprs.2014.09.015

Neugirg, F., Stark, M., Kaiser, A., Vlácilová, M., Della Seta, M., Vergari, F., … Haas, F. (2016). Erosion processes in calanchi in the Upper Orcia Valley, Southern Tuscany, Italy based on multitemporal high-resolution terrestrial LiDAR and UAV surveys. *Geomorphology, 269*, 8–22. https://doi.org/10.1016/j.geomorph.2016.06.027

Obanawa, H., & Hayakawa, Y. S. (2018). Variations in volumetric erosion rates of bedrock cliffs on a small inaccessible coastal island determined using measurements by an unmanned aerial vehicle with structure-from-motion and terrestrial laser scanning. *Progress in Earth and Planetary Science, 5*(1), 33. https://doi.org/10.1186/s40645-018-0191-8

Olaya, V. (2014). *Module filter clumps*. Retrieved from https://libguides.library.usyd.edu.au/c.php?g=508212&p=3476096

Paranunzio, R., Laio, F., Chiarle, M., Nigrelli, G., & Guzzetti, F. (2016). Climate anomalies associated with the occurrence of rockfalls at high-elevation in the Italian Alps. *Natural Hazards and Earth System Sciences, 16*(9), 2085–2106. https://doi.org/10.5194/nhess-16-2085-2016

Pfeiffer, T. J., & Bowen, T. D. (1989). Computer simulations of rockfalls. *Environmental & Engineering Geoscience, xxvi* (1), 135–146. https://doi.org/10.2113/gseegeosci.xxvi.1.135

Ravanel, L., & Deline, P. (2008). The West Face of Les Drus (Mont-Blanc massif): slope instability in a high-Alpine steep rock wall since the end of the Little Ice Age. *Géomorphologie: Relief, Processus*. *Environnement, 4*, 261–272.

Ravanel, L., & Deline, P. (2010). Climate influence on rockfalls in high-Alpine steep rockwalls: The north side of the Aiguilles de Chamonix (Mont Blanc massif) since the end of the 'Little Ice Age'. *The Holocene, 21*(2), 357–365. https://doi.org/10.1177/0959683610374887

Ravanel, L., Allignol, F., Deline, P., Gruber, S., & Ravello, M. (2010). Rock falls in the Mont Blanc massif in 2007 and 2008. *Landslides, 7*(4), 493–501. https://doi.org/10.1007/s10346-010-0206-z

RIEGL Laser Measurement Systems GmbH (2020). *RIEGL VZ-4000*. Retrieved from http://www.riegl.com/uploads/tx_pxpriegldownloads/RIEGL_VZ-4000_Datasheet_2020-09-14.pdf

Royán, M. J., Abellán, A., Jaboyedoff, M., Vilaplana, J. M., & Calvet, J. (2014). Spatio-temporal analysis of rockfall pre-

failure deformation using Terrestrial LiDAR. *Landslides, 11*(4), 697–709. https://doi.org/10.1007/s10346-013-0442-0

Sala, Z., Hutchinson, D. J., & Harrap, R. (2019). Simulation of fragmental rockfalls detected using terrestrial laser scans from rockslopes in south-central British Columbia, Canada. *Natural Hazards and Earth System Sciences, 19*(11), 2385–2404. https://doi.org/10.5194/nhess-19-2385-2019

Salvini, R., Francioni, M., Riccucci, S., Bonciani, F., & Callegari, I. (2013). Photogrammetry and laser scanning for analyzing slope stability and rock fall runout along the Domodossola-Iselle railway, the Italian Alps. *Geomorphology, 185*, 110–122. https://doi.org/10.1016/j.geomorph.2012.12.020

Sanz-Ablanedo, E., Chandler, J. H., Rodríguez-Pérez, J. R., & Ordóñez, C. (2018). Accuracy of Unmanned Aerial Vehicle (UAV) and SfM photogrammetry survey as a function of the number and location of ground control points used. *Remote Sensing (Basel), 10*(10), 1606. https://doi.org/10.3390/rs10101606

Stark, M., Rom, J., Haas, F., Piermattei, L., Fleischer, F., Altmann, M., & Becht, M. (2022). Long-term assessment of terrain changes and calculation of erosion rates in an alpine catchment based on SfM-MVS processing of historical aerial images. How camera information and processing strategy affect quantitative analysis. *Journal of Geomorphology, 1*(1), 43–77. https://doi.org/10.1127/jgeomorphology/2022/0755

Strunden, J., Ehlers, T. A., Brehm, D., & Nettesheim, M. (2015). Spatial and temporal variations in rockfall determined from TLS measurements in a deglaciated valley, Switzerland. *Journal of Geophysical Research. Earth Surface, 120*(7), 1251–1273. https://doi.org/10.1002/2014JF003274

Stumpf, A., Malet, J.-P., Allemand, P., Pierrot-Deseilligny, M., & Skupinski, G. (2015). Ground-based multi-view photogrammetry for the monitoring of landslide deformation and erosion. *Geomorphology, 231*, 130–145. https://doi.org/10.1016/j.geomorph.2014.10.039

Tonkin, T. N., & Midgley, N. G. (2016). Ground-control networks for image based surface reconstruction: An investigation of optimum survey designs using UAV derived imagery and structure-from-motion photogrammetry. *Remote Sensing (Basel), 8*(9), 786. https://doi.org/10.3390/rs8090786

Torres-Sánchez, J., López-Granados, F., Borra-Serrano, I., & Peña, J. M. (2018). Assessing UAV-collected image overlap influence on computation time and digital surface model accuracy in olive orchards. *Precision Agriculture, 19*(1), 115–133. https://doi.org/10.1007/s11119-017-9502-0

Ullman, S. (1979). The interpretation of structure from motion. *Proceedings of the Royal Society of London. Series B, Biological Sciences, 203*(1153), 405–426. https://doi.org/10.1098/rspb.1979.0006

Vanneschi, C., Di Camillo, M., Aiello, E., Bonciani, F., & Salvini, R. (2019). SfM-MVS photogrammetry for rockfall analysis and hazard assessment along the ancient Roman Via Flaminia road at the Furlo Gorge (Italy). *ISPRS International Journal of Geo-Information, 8*(8), 325. https://doi.org/10.3390/ijgi8080325

Verma, A. K., & Bourke, M. C. (2019). A method based on structure-from-motion photogrammetry to generate sub-millimetre-resolution digital elevation models for investigating rock breakdown features. *Earth Surface Dynamics, 7*(1), 45–66. https://doi.org/10.5194/esurf-7-45-2019

Viero, A., Furlanis, S., Squarzoni, C., Teza, G., Galgaro, A., & Gianolla, P. (2013). Dynamics and mass balance of the 2007 Cima Una rockfall (Eastern Alps, Italy). *Landslides, 10*(4), 393–408. https://doi.org/10.1007/s10346-012-0338-4

Vivero, S., & Lambiel, C. (2019). Monitoring the crisis of a rock glacier with repeated UAV surveys. *Geographica Helvetica, 74*(1), 59–69. https://doi.org/10.5194/gh-74-59-2019

Volkwein, A., Schellenberg, K., Labiouse, V., Agliardi, F., Berger, F., Bourrier, F., … Jaboyedoff, M. (2011). Rockfall characterisation and structural protection – a review. *Natural Hazards and Earth System Sciences, 11*(9), 2617–2651. https://doi.org/10.5194/nhess-11-2617-2011

Warrick, J. A., Ritchie, A. C., Adelman, G., Adelman, K., & Limber, P. W. (2017). New techniques to measure cliff change from historical oblique aerial photographs and structure-from-motion photogrammetry. *Journal of Coastal Research, 33*(1), 39–55. https://doi.org/10.2112/JCOASTRES-D-16-00095.1

Westoby, M. J., Brasington, J., Glasser, N. F., Hambrey, M. J., & Reynolds, J. M. (2012). 'Structure-from-Motion' photogrammetry: A low-cost, effective tool for geoscience applications. *Geomorphology, 179*, 300–314. https://doi.org/10.1016/j.geomorph.2012.08.021

Zhang, Z. (1994). Iterative point matching for registration of free-form curves and surfaces. *International Journal of Computer Vision, 13*(2), 119–152. https://doi.org/10.1007/BF01427149

Manuscript received: October 21, 2022
Revisions requested: March 28, 2023
Revised version received: May 19, 2023
Accepted: May 19, 2023